



**HAL**  
open science

# The role of lateral branches on effective stiffness and local overstresses in dentin

Elsa Vennat, Asef Hemmati, Nicolas Schmitt, D. Aubry

► **To cite this version:**

Elsa Vennat, Asef Hemmati, Nicolas Schmitt, D. Aubry. The role of lateral branches on effective stiffness and local overstresses in dentin. *Journal of the mechanical behavior of biomedical materials*, 2021, 116, pp.104329. 10.1016/j.jmbbm.2021.104329 . hal-03249482

**HAL Id: hal-03249482**

**<https://hal.science/hal-03249482>**

Submitted on 13 Feb 2023

**HAL** is a multi-disciplinary open access archive for the deposit and dissemination of scientific research documents, whether they are published or not. The documents may come from teaching and research institutions in France or abroad, or from public or private research centers.

L'archive ouverte pluridisciplinaire **HAL**, est destinée au dépôt et à la diffusion de documents scientifiques de niveau recherche, publiés ou non, émanant des établissements d'enseignement et de recherche français ou étrangers, des laboratoires publics ou privés.



Distributed under a Creative Commons Attribution - NonCommercial 4.0 International License

# The role of lateral branches on effective stiffness and local overstresses in dentin

Elsa Vennat<sup>1</sup>, Asef Hemmati<sup>1,2</sup>, Nicolas Schmitt<sup>2,3</sup>, Denis Aubry<sup>1</sup>

<sup>1</sup> Université Paris-Saclay, CentraleSupélec, CNRS, Laboratoire de Mécanique des Sols, Structures et Matériaux, 91190, Gif-sur-Yvette, France.

<sup>2</sup> Université Paris-Saclay, ENS Paris-Saclay, CNRS, Laboratoire de Mécanique et de Technologie, 91190, Gif-sur-Yvette, France.

<sup>3</sup> Université Paris-Est Créteil, Inspé, 93203 Saint-Denis, France

## Abstract

The 3D microstructure of dentinal tissue, the main tissue of the tooth, is the subject of an increasingly comprehensive body of knowledge. The relationship between this microstructure and the mechanical behaviour of dentinal tissue remains, nonetheless, under question. This article proposes an original SEM analysis of dentin microstructure, accounting for lateral branches, and a mechanical model based on these findings. An interesting observation is that lateral branches have a dense collar, as do tubules. The diameter of these branches as well as a percentage area are quantified all along the depth of a dentin sample. We use these unprecedented data to build an orthotropic homogenized model of dentin. The heterogeneities of microstructure are taken into account using level-set functions. The results reveal that the lateral branches slightly influence the global homogenized elastic behavior of the dentin tissue, albeit creating stress concentration areas that are highly influenced by the inclination of the traction with respect to the tubule and branches.

## 1. Introduction

The tooth is a sensitive biomechanical structure, which must provide sufficient stiffness and strength, simultaneously, to fragment hard food with the crown at one end without compromising support to the gingiva at the other end. The tooth's stiffness must thus vary gradually from enamel to pulp cavity. This stiffness acts as a sensor through the nerve, informing the mandibular muscle to control pressure levels in order to break down food. The living cushion which provides said stiffness gradient is known as the dentin.

Dentin material is thus a key tissue inside the tooth; the main tissue in terms of volume and the tissue on which most dental restorations are bonded. The restorative materials have to replace it as durably as possible. Given that most of the world's population experiences dental problems at least once a lifetime, deeper knowledge of dentinal tissue is crucial. The scientific challenge of deepening this knowledge is geared towards linking both, knowledge of its microstructure and knowledge of its mechanical properties.

Dentin is a complex porous medium with microstructural gradients in depth (millimetric length scale). Most of the time, however, dentin is simplified being indeed alluded to as a triphasic structure (micrometric length scale) with tubules (cylindrical voids called lumens (L), encircled by a peritubular collar called peritubular dentin, (PTD) and intertubular dentin (ITD), Figure 1) (Kinney *et al.* 2003).

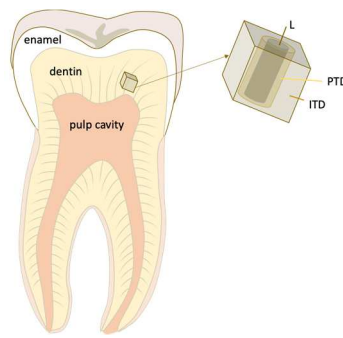


Figure 1 : Classical representation of a tooth and of the dentin microstructure

Dentin's contribution to the total porosity of channels other than tubules are non-negligible, as recently demonstrated. Such channels also greatly contribute to the maximum stress in the tissue (Vennat et al. 2017). The auxiliary channel network, classified by Mjor and Nordahl (1996), is made up of different types of lateral branches (LB) near the enamel:

- major branches (0.5-1 $\mu$ m diameter) fused to become tubules when moving towards the middle dentin;
- fine branches (0.3-0.7 $\mu$ m diameter), quantified in Vennat et al. 2017, form an angle of roughly 45° with the tubules

In middle dentin, microbranches (0.025-0.2 $\mu$ m diameter) are observed and rise at right angle with the tubules. To our knowledge, however, no information is available on their volume ratios or size distribution. We may wonder if a highly mineralized collar is surrounding these lateral branches.

We first investigate the dentinal tissue by SEM (Scanning Electron Microscopy). This investigation quantifies the variation of characteristics in sub-structures (L, ITD, PTD, LBC and LBL, LBL or lateral branch lumen) within the tissue (from pulp to enamel), highlighting morphological features potentially influencing the global and local mechanical properties of dentin. We then build a mechanical model of the dentinal tissue in light of our findings. A periodic model of dentin is presented considering the LB (LBL and LBC), observed by SEM. The model's uniqueness is that the geometrical entities are not meshed explicitly, allowing for the direct use of images to quantify the dentin mechanical behavior. The model leads to an assessment of the equivalent stiffness tensor, together with a micromechanical failure criterion.

## 2. Previous theoretical and numerical models of dentin

67  
68  
69  
70  
71  
72  
73  
74  
75  
76  
77  
78  
79  
80  
81  
82  
83  
84  
85  
86  
87  
88  
89  
90  
91  
92  
93  
94  
95  
96  
97  
98  
99  
100  
101  
102  
103  
104  
105  
106  
107  
108  
109  
110  
111  
112

In previous numerical or theoretical studies of the dentinal tissue, only results and the tubular structure accounting for dentin porosity (Kinney et al. 1999, Qin & Swain 2004, Bar-On & Wagner 2012, Yoon et al. 2013, Wang et al. 2017 and Arson et al. 2019) were presented in terms of effective properties.

Kinney et al. (1999) proposed an initial micromechanical model considering ITD, PTD and L and claimed that the matrix (ITD) dominates the elastic mechanical behavior of bulk dentin. Qin & Swain (2004) also developed a model considering dentin as an assembly of ITD, PTD and L with different volume ratios and local elastic modulus. An interesting finding is that the modulus parallel to the tubules is always higher than the modulus perpendicular to the tubules; both decrease with distance to pulp. Bar-On & Wagner (2012) were the first to model the scale of the entanglement between collagen fibrils and the aforementioned hydroxyapatite crystals for ITD, as a staggered platelet micro-structure. The tissue consisting of ITD, PTD and L were then studied, revealing that the modulus parallel to the tubules can be lower than the modulus perpendicular to the tubules, showing the impact of the lower scale structure. They further discovered that a transition from isotropy to anisotropy arises depending on location in the dentin. Yoon et al. (2013) proposed two geometrical scales of homogenization: at the lowest scale, ITD is considered as a mixture of collagen fibrils, hydroxyapatite crystals (which are considered as plate-shaped or needle-shaped) and water, and at the highest scale, dentin is considered as a periodic composite made of ITD, PTD and L. More recently, Seyedkavoosi & Sevostianov (2019) attempted to study the anisotropy of hydroxyapatite crystals and assessed its influence on effective mechanical properties.

In terms of geometric modeling, Wang et al. (2017) and Arson et al. (2019) are of particular interest in that SEM images are used to better take into account the real microstructure of dentin (L, PTD and ITD) whereas the other authors are using data from the literature.

In these previous studies, to the best of our knowledge, the effect of LB was not investigated. We claim that these branches and their possible mineralized collar (known as the lateral branch collar, LBC) have a significant role in the mechanical behavior of dentin. Analysis of the local stress field is also crucial towards deducing the location of crack initiation, for example, which is often overlooked in the literature.

As quantitative experimental data on LB is lacking, we propose an experimental protocol to assess the sizes and surface ratios of the dentinal microstructure features including the LB. Using this protocol, we estimate the ratio of PTD, ITD, L and LBC in three locations of a dentin-sample.

Apart from geometry, other input data for the model are the local mechanical properties. At the submicron scale, the properties of individual collagen fibrils and hydroxyapatite crystals are not accurately known. As crucial interface properties remain unknown and the mixture organization remains under debate, this scale is not taken into account. In the discussion, we explain how the lower scale can be included in this model in future studies.

At the scale of tissue features, more data are available. The PTD elastic stiffness appears isotropic (Ziskind et al. 2011 with an elastic modulus usually set between 20 and 40GPa in the mechanical models. Kinney et al. (1996) estimate 29.8GPa as its lower limit. The ITD is slightly anisotropic and its elastic modulus varies between 17.7 and 21.1GPa depending on the location in the tissue (Kinney et al. 1996). Little information is available in

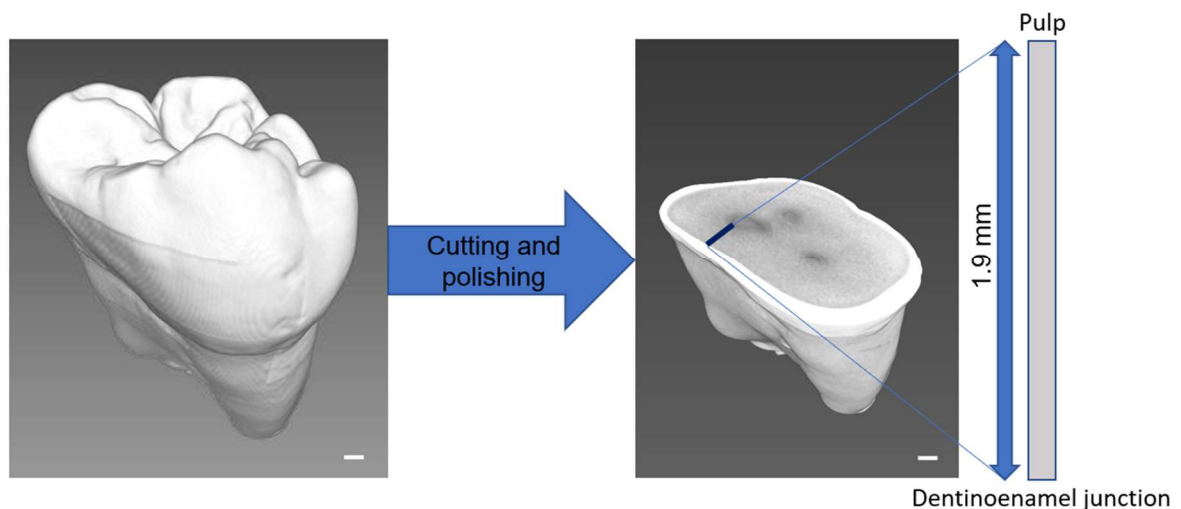
113 the literature concerning the possible presence of collar of lateral branches and their  
 114 stiffness. Only Zanette et al. (2015) mentioned a dense collar surrounding LB. As we want to  
 115 focus on the LB impact in this study, only the tissue scale will be investigated numerically.

116 Dentin strength and toughness are also influenced by the hierarchical structure of this  
 117 material (Iwamoto & Ruse 2003, Nalla et al. 2003, Arola et al. 2005, Han et al. 2012, Eltit et  
 118 al. 2017, Lu et al. 2018 and Lu et al. 2019). The tubule orientation and the ITD organization  
 119 impact are discussed in the literature although the LB impact is not discussed. The models of  
 120 crack propagation proposed by An and Wagner (2016) and An et al. (2017) take into account  
 121 only the tubules in a 2D model. The different authors agree that voids corresponding to  
 122 tubule lumens and the PTD are important microstructural entities whose properties and  
 123 ratios influence failure. LB and their collars play a defining role in dentin failure.

### 124 3. Image analysis protocol

#### 125 3.1. Images data

126 A sound human third molar of a young adult (obtained with donor consent) was  
 127 embedded in epoxy resin and imaged using microcomputed tomography (Quantum FX  
 128 Perkin Elmer, with a pixel size of 50 $\mu$ m). The embedded tooth was then cut (ISOMET Low  
 129 Speed Saw, Buehler) in order to reveal a coronal surface (Figure 1), where the dentin  
 130 showed an interface both with enamel and pulp cavity. The surface was polished with  
 131 polishing disks of decreasing grid size (LaboPol-5, Struers) and the final polishing was  
 132 achieved using a polishing cloth and a 1  $\mu$ m diamond suspension (TegraPol-15, Struers).



133 Between each polishing step, the sample was cleaned in an ultrasonic bath.

134

135 *Figure 2 : 3D visualization of the selected tooth (reconstructed from microCT images) before (A) and after polishing (B). SEM*  
 136 *image locations are indicated in B (scale bar: 1 mm).*

#### 137 3.2. SEM imaging

138 For scanning electron microscopy, the sample was dehydrated using ethanol bath with  
 139 an increasing concentration. The microstructure of dentin was imaged using  
 140 Helios Nanolab 660 (FEI). Backscattered electrons (BSE) detector was used in order to reveal

141 the chemical contrast between the highly mineralized peritubular dentin and the less  
142 mineralized inter-tubular dentin.

143 To study the local variation of the morphological properties, one image was acquired  
144 close to the enamel (E), one in the middle dentin (M) and one close to the pulp (P) at  
145 distances of 250, 1000 and 1850  $\mu\text{m}$  from dentino-enamel junction (DEJ) respectively (Figure  
146 1).

147 Some interesting areas at higher magnifications have also been imaged using a FEG-  
148 SEM (Zeiss Supra 55 VP) in BSE mode on the same polished surface.

### 149 **3.3. Image treatment and analysis**

150 The software “FIJI” (Schneider et al. 2012 and Schindelin et al. 2012) was used  
151 for image analysis. First, brightness and contrast of the images were self-  
152 adjusted. Then, Weka plugin (Arganda-Carreras et al. 2017) of FIJI was used to segment the  
153 images (Figure 2).

154 The image was segmented into three classes: 1) lumen L inside tubules -in black- 2)  
155 bright and highly mineralized parts PTD and LBC -shown in white- 3) intertubular dentin ITD -  
156 in grey-. Once the image was segmented, it was manually edited and median filtered to  
157 remove the noise. Finally, the segmented images, were turned into three binary images  
158 using “adjust threshold”. Each binary image represents one of the classes. From these  
159 images, each constituent surface ratio is assessed.

160

161

162 *Figure 3 : The image processing protocol illustrated for a part of the image M (scale bar: 5  $\mu\text{m}$ ). The constituents of dentin*  
163 *are marked: Lumen (L), peritubular dentin (PTD), intertubular dentin (ITD) and lateral branch collars (LBC).*

164 It should be noted that this highly mineral phase consists in PTD and LBC. The protocol  
165 for quantifying the highly mineralized phase is shown in Figure 3. The dimensions of these  
166 parts are measured using the “Analyze Particles” tool in FIJI.

167

168

169

170

*Figure 4 : The protocol for studying the highly mineralized parts of dentin from the treated image*

171 The “Analyze particles” enables to assess the number of particles (here tubules and  
172 LB), from which the density can be calculated and the diameters of the considered structural  
173 entities (Figure 4).

## 174 **4. Periodic homogenization and numerical method**

175 Our aim here is to account for a truly 3D micro geometry with transverse open and  
176 reinforced channels.

177 The homogenization approach has been more than extensively used to predict  
178 equivalent material properties at a large scale from heterogeneities at a smaller scale  
179 avoiding thus multi-scale strong coupling. The different assumptions may roughly be  
180 grouped according to the Elementary Volume Approach (Christensen 2005) where either  
181 macro-strains or stresses are given as boundary conditions and equivalent stiffness or  
182 compliance tensors are derived by averaging, or the Multiple Scale Method with periodicity  
183 assumptions (Sanchez-Palencia 1980, Cioranescu & Donato 1999)

184 We are particularly interested by the case of thin channels and refer to different  
 185 studies by Cioranescu & Donato (1999) for reticulated structures where not only the  
 186 reference volume is small with respect to the structural scale but furthermore the  
 187 constituents are very thin inside this reference volume. Taking into account a 3D geometry  
 188 like the one extracted from the images presented in the first section of this work requires  
 189 usually to use a numerical approach because exact solutions are available only for simple  
 190 geometries like embedded spheres or cylinders with moreover the assumptions of dilute  
 191 concentration.

192 The typical geometry that is considered here is a periodic brick with a cylindrical tubule  
 193 along one axis and four cylindrical lateral branches along the other two perpendicular axis  
 194 (Figure 5).

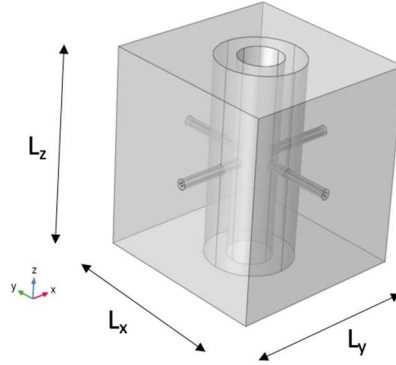


Figure 5 : The considered periodic cell

195  
196

#### 4.1. The rapidly oscillating elasticity tensor

197  
198 The 4<sup>th</sup> order elasticity tensors of the different materials are given by  $C_n$  with  $n=m$  for  
 199 the matrix (ITD),  $n=c$  for the collar materials (PTD and LBC) and  $n=v$  for the empty channels (L  
 200 and LBL). The representation of these tensors may be given with the help of their  
 201 characteristic functions. Calling  $r = \sqrt{x^2 + y^2}$  and  $r_e$  and  $r_i$  respectively the outer and inner  
 202 collar radii resting in the plane  $x$ - $y$  with  $z$ -axis, the characteristic function of this  $x$ - $y$  tubular  
 203 collar is:  $\chi_z(X) = H(-|r - \frac{r_e+r_i}{2}| + \frac{r_e-r_i}{2})$  with  $H$  the classical Heaviside, or unit step,  
 204 function and  $X = \{x, y, z\}$ . Similar characteristic functions are built for the other collars  
 205 including the void inside the tubules. From the latter, it is possible to build the characteristic  
 206 functions for the Boolean intersection and union of different parts such as the ensemble of  
 207 all the collars and the ensemble of the whole empty zone inside the channels. For example,  
 208 the characteristic function of the union of all the collars is obtained by using the maximum of  
 209 these functions and the intersection the minimum. Finally, the elasticity tensor of the  
 210 heterogeneous dentin material may be represented by:

$$C(X) = \chi_m(X)C_m + \chi_c(X)C_c + \chi_v(X)C_v$$

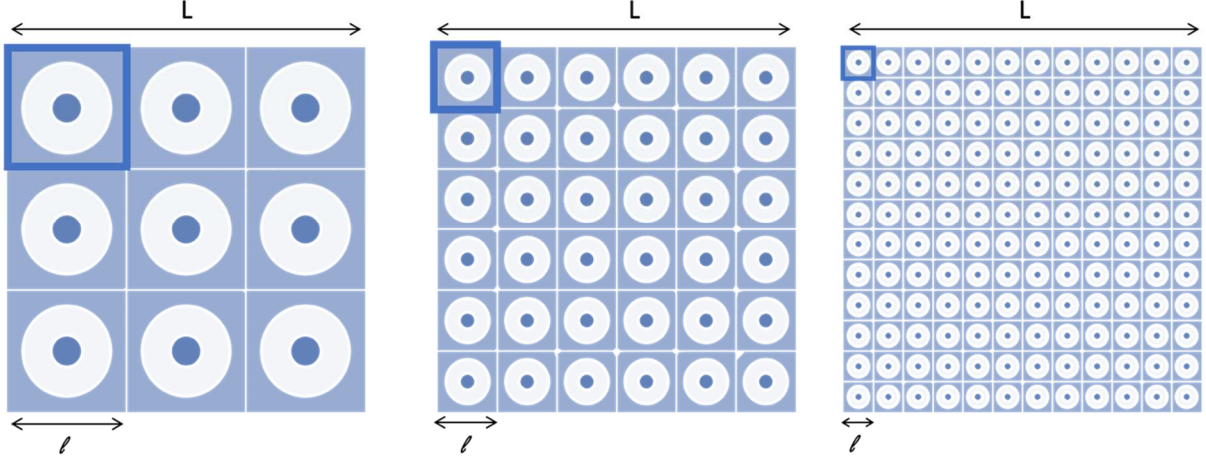
211  
212 With  $\chi_m, \chi_c$  and  $\chi_v$  the characteristic functions of the ITD, PTD+LBC and void. Now let  
 213  $L \cong 2mm$ , be a characteristic size of the dentin domain and  $l \cong 10\mu m$  the length of the  
 214 periodic cell. It is interesting to define the scale parameter  $\xi = l/L$  and to parametrize the  
 215 geometry of the cell with respect to it. We can define  $\bar{r}_i$  and  $\bar{r}_e$  so that:  $r_e = \xi \bar{r}_e$  and  $r_i = \xi \bar{r}_i$   
 216 such that the characteristic function  $\chi_z$  may be equivalently be written:

$$217 \quad \chi_z\left(\frac{X}{\xi}\right) = H\left(-\left|\frac{r}{\xi} - \frac{\bar{r}_e + \bar{r}_i}{2}\right| + \frac{\bar{r}_e - \bar{r}_i}{2}\right)$$

218 This scale parametrization leads to the following expression for the elasticity tensors:

$$219 \quad C\left(\frac{X}{\xi}\right) = \chi_m\left(\frac{X}{\xi}\right) C_m + \chi_c\left(\frac{X}{\xi}\right) C_{Pc} + \chi_v\left(\frac{X}{\xi}\right) C_v$$

220 with  $C$ , a periodic function of  $\frac{X}{\xi}$ . A 2D illustration of the characteristic function of the  
 221 heterogeneous material is given Figure 6 for different values of the period  $l$ .



222  
 223 *Figure 6 : 2D illustration of different microstructures with decreasing  $l$  and  $\xi$  (the cell  $Y$  is underlined in blue) also*  
 224 *corresponding to the values of the  $C$  function (the darker area corresponds to  $C_v$  and the lighter to  $C_c$ )*

225 Now when the whole tooth undergoes a chewing loading, the dentin material itself  $\Omega_d$   
 226 is submitted to a macroscopic load from the enamel and the anchorage tissue. Ignoring body  
 227 forces, the corresponding elasticity equations read where, for notation simplification  
 228 purposes,  $X$  is replaced by  $x$ :

$$229 \quad \begin{cases} \text{Div } C\left(\frac{x}{\xi}\right) : \varepsilon(u) = 0 & \text{in } \Omega_d \\ C\left(\frac{x}{\xi}\right) : \varepsilon(u) \cdot n = f_s & \text{on the loaded boundaries} \\ C\left(\frac{x}{\xi}\right) : \varepsilon(u) \cdot n = 0 & \text{at the boundary with the tubule lumen} \end{cases}$$

230  
 231 With  $\text{Div}$  the classical divergence operator for the stresses,  $u$  the displacements,  $\varepsilon$   
 232 the small strain tensor,  $f_s$  is the surface force applied on the enamel by the tooth in contact  
 233 and  $n$  the unit outwards normal to the dentin boundary. It is assumed here that the channels  
 234 are not filled with any interstitial fluid although this hypothesis can be easily taken into  
 235 account by an additional term which would lead to poroelastic properties.

#### 236 **4.2. The two-scales series expansion**

237 Due to the sizes of the peritubular and lateral branches heterogeneities are small with  
 238 respect to the size of the whole dentin domain, this problem cannot be solved numerically  
 239 economically (Sanchez-Palencia 1980). The classical *ansatz* provided by the multiple scale  
 240 approach is to solve this problem approximately by looking for a two scales series expansion

241  $u_m\left(x, \frac{x}{\xi}\right)$  of the displacement, each term being periodic with respect to the second variable.

242 Calling  $y = \frac{x}{\xi}$ , the second independent variable, then computing the total derivatives of the  
 243 strains-displacements and equilibrium equations, make the scale  $\xi$  explicitly appear, which is  
 244 a key point:

$$245 \quad \begin{cases} \varepsilon(u) = \varepsilon_x(u) + \frac{1}{\xi} \varepsilon_y(u) \\ Div \sigma = Div_x \sigma + \frac{1}{\xi} Div_y \sigma \end{cases}$$

246 By plugging the series into the elasticity problem above, different powers of  $\xi$  appear  
 247 so that by cancelling each coefficient, successive elasticity problems need to be solved.  
 248 Considering only the first three terms is enough for the homogenization process. Indeed, the  
 249 first equation shows that  $u_0$  does not depend on  $y$ . The second one gives  $u_1$  as the periodic  
 250 microscopic solution of a macroscopic initial strain -  $\varepsilon_x(u_0)$  problem:

$$251 \quad Div_y C : (\varepsilon_y(u_1) + \varepsilon_x(u_0)) = 0$$

252 Because of the linearity this equation shows that there exists a fourth-order tensor  $A$ ,  
 253 usually called the strain localization tensor such that:

$$254 \quad \varepsilon_y(u_1) = A(y) : (\varepsilon_x(u_0))$$

255 At last, the third equation, integrated over the cell  $Y$  (indicated on the 2D  
 256 microstructures in Figure 6), taking into account the periodic boundary conditions at the  
 257 boundary of the cell  $Y$  (Sanchez Palencia 1980, Cioranescu & Donato 1999), eliminates  $u_2$  and  
 258 gives the macroscopic problem that  $u_0$  has to satisfy:

$$259 \quad Div_x \langle C(I + A) \rangle : \varepsilon_x(u_0) = 0$$

260 Where  $\langle \cdot \rangle$  stands for the average over the microscopic cell  $Y$ . The last equation allows  
 261 to identify the macroscopic stiffness tensor  $\tilde{C}$ . We define it implicitly by its action on a  
 262 uniform macro-strain  $E$  from which its components may then be easily recovered:

$$264 \quad \tilde{C} : E = \frac{1}{vol(Y)} \int_Y C : ((I + A) : E) dV_y$$

266 A virtual work formulation leads classically to the usual major and minor symmetries of  
 267  $\tilde{C}$ .

### 268 **4.3. The orthotropy of the homogenized elasticity tensor**

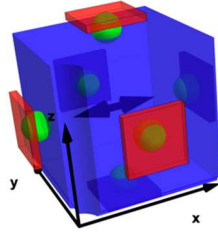
269 As mentioned above, the elastic problems which provides  $A$  satisfies the following  
 270 equilibrium equation with initial uniform strain -  $E$ :

$$271 \quad Div_y C : (\varepsilon_y(E) + E) = 0$$

272 Periodic boundary conditions (and also vanishing average displacements to avoid rigid  
 273 body translations), have to be considered. However, when the stiffness tensor and the  
 274 geometry of the periodic cell satisfy given symmetry conditions, the corresponding solution  
 275 inherits itself some symmetry which can sometimes implies periodicity. Here we assume  
 276 that the constituents materials are elastic isotropic so that the geometry of the cell is

277 endowed with three orthogonal planes of symmetry from which it can be concluded that  $\tilde{\mathcal{C}}$   
 278 satisfies orthotropic symmetries.

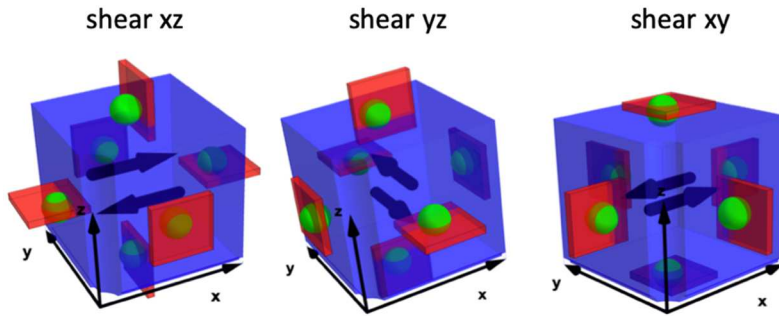
279 Going one step further, the geometric symmetry allows to decrease the size of the  
 280 elementary cell to one eighth with specific boundary conditions. For an extensional



281 initial strain, thanks to both periodicity and mirror symmetries along the middle symmetry  
 282 planes, the normal displacement and the shear stress must vanish. Along the outer  
 283 boundary of the periodic cell, the same boundary conditions prevail (Figure 7).

284  
 285

Figure 7: Boundary conditions for the three extensions



286  
 287

Figure 8 : the three shear boundary conditions

288 The boundary conditions for an initial shear strain along the symmetry planes are  
 289 different: the perpendicular displacement to the macroscopic shear plane and the  
 290 corresponding shear stress must vanish and along the boundary of the periodic cell, the  
 291 same boundary conditions prevail (

292 Figure 8). Because of these symmetries, the average displacement in each case  
 293 vanishes so that all the equations of the periodic problem inside and at the boundary of the  
 294 whole cell are satisfied.

295 From  $\tilde{\mathcal{C}}$ , the orthotropic homogenized compliance  $\tilde{\mathcal{S}} = \tilde{\mathcal{C}}^{-1}$  is finally obtained from  
 296 which engineering coefficients like Young's moduli and Poisson ratios are easily recovered:

297

$$298 \left\{ \begin{array}{l} \tilde{S}_{xxxx} = \frac{1}{E_x}, \tilde{S}_{xxyy} = -\frac{\nu_{xy}}{E_x}, \tilde{S}_{xxzz} = -\frac{\nu_{xz}}{E_x} \\ \tilde{S}_{xyxy} = \frac{1}{2G_{xy}} \end{array} \right.$$

299 With obvious notations for the other components.

#### 4.4. Microscopic maximal traction under given macroscopic oriented uniaxial traction

300  
301

302 As a final step of the model development, we want to show how the approach allows  
303 also to exhibit a failure criterion under macroscopic tension. The failure criterion of the  
304 homogenized dentin tissue comes from local failure criterion at the scale of the periodic cell  
305  $Y$ . Following Christensen (2013) the local maximum traction is considered since the mineral  
306 collars are particularly sensitive to tension. Other microscopic criteria can be considered as  
307 well following the same arguments. If we look back at the above development of the two-  
308 scale approach the local micro stress tensor is given from a product of a strain concentration  
309 tensor  $A$  and the macroscopic strain  $\varepsilon_{x0} = \varepsilon_x(u_0)$ :

$$310 \quad \sigma_y = C : (A : \varepsilon_{x0} + \varepsilon_{x0})$$

311 Let  $\sigma_0 e_0 \otimes e_0$  be an applied macroscopic uniaxial tension with amplitude  $\sigma_0$  along the unit  
312 axis  $e_0$  defined by two angles  $(\theta_0, \varphi_0)$ . Then the macroscopic strain  $\varepsilon_{x0}$  is given by  
313  $\varepsilon_{x0} = \sigma_0 \tilde{S}(e_0 \otimes e_0)$  and the local micro-stress by:

314

$$315 \quad \sigma_y = \sigma_0 C : (I + A) : \tilde{S}(e_0 \otimes e_0) = \sigma_0 \Sigma_y(\theta_0, \varphi_0)$$

316 With  $\Sigma_y(\theta_0, \varphi_0)$  representing the factor of  
317  $\sigma_0$  in the second right-hand side of the above equation. Now, if we define the following  
318 invariants of  $\sigma_y$  and its deviatoric part  $\sigma_y^D$  :

319

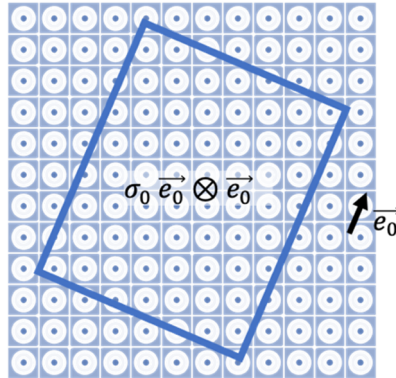
$$320 \quad \left\{ \begin{array}{l} I_1 = Tr(\sigma_y) \\ J_2 = \frac{1}{2} Tr(\sigma_y^D)^2 \\ J_3 = \frac{1}{3} Tr(\sigma_y^D)^3 \\ \psi = \frac{1}{3} \arcsin\left(-\frac{3\sqrt{3}}{2} \frac{J_3}{J_2^{\frac{3}{2}}}\right) \end{array} \right.$$

321 The major principal micro-stress is given by (see e.g. Zienkiewicz et al. 1999):

322

$$323 \quad \sigma_{max} = \frac{I_1}{3} + \frac{2\sqrt{J_2}}{\sqrt{3}} \sin\left(\psi + \frac{2\pi}{3}\right)$$

324



325

Figure 9 : Illustration in 2D of the considered loading

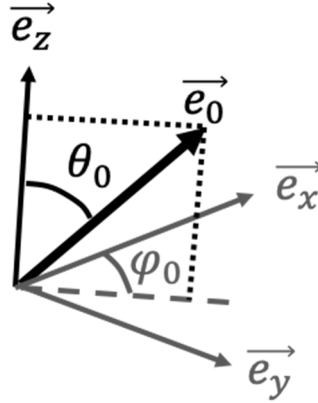
326  
327

Figure 10 : The considered coordinate system

328 Using the preceding formulas, it is easy to demonstrate that  $\sigma_{max}$  is a linear function  
 329 of the amplitude of the applied macro-stress  $\sigma_0$  and an algebraic function  $\Sigma_m$  of the two  
 330 angles  $(\theta_0, \varphi_0)$  (Figure 10):

$$331 \quad \sigma_{max} = \sigma_0 \Sigma_m(\theta_0, \varphi_0)$$

332 When the maximal traction of the collar material  $\sigma_T$  is reached usually along the  
 333 boundary with the lumen, the corresponding maximal value of  $\sigma_0$ , the amplitude of the  
 334 macro-stress is obtained:

$$335 \quad \sigma_0 \leq \frac{\sigma_T}{\Sigma_m(\theta_0, \varphi_0)}$$

336 However, we show in the paragraph dedicated to the results that, depending on the  
 337 orientation of the macroscopic traction, the maximum principal stress may be located in  
 338 different areas. This leads us to consider several inequalities and criteria of the above type,  
 339 correspondingly. Thus, the macroscopic failure criterion depends on the orientation of the  
 340 network with respect to the applied macro-stress while this orientation varies inside the  
 341 dentin from the pulp to the enamel. At local scale, a crack may eventually open  
 342 perpendicular to the hole boundary. This macroscopic failure criterion shares a certain  
 343 similarity with the classical Schmid's law although issued from different microscopic reasons.  
 344 Here a simple macro-tension has been considered but the case of a full macro-stress is easily  
 345 designed along the same lines.

346

#### 4.5. Numerical method

347 The above considerations show that two computations must be handled:

- 348 (1) the average of the micro-stress inside the cell  $Y$  to get the equivalent macro-moduli
- 349 (2) the local stress concentration of the maximum principal stress.

350 Both computations are implemented by the Finite Element Method. But rather than  
 351 building a mesh from the geometry of the periodic cell, it is preferred to use a Level Set  
 352 approach mixed with a mesh adaptation with a quantity of interest (Bangerth & Rannacher  
 353 2003) so that only one eighth part of the  $Y$ -cell is loosely meshed and heterogeneous zones  
 354 are identified by their smoothed characteristic functions  $\chi_n^s$  with  $n = \{m|c|v\}$  defined by:

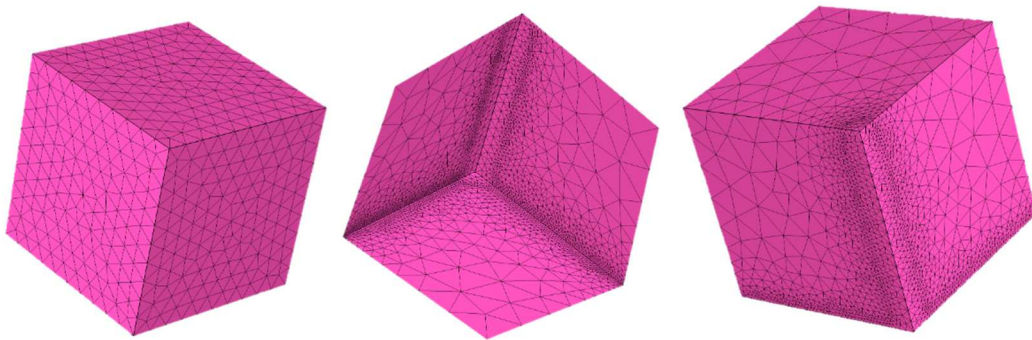
$$\chi_n^s(x, \delta) = \begin{cases} 0 & \text{if } x < -\delta \\ \frac{1}{2}(1 + \frac{3}{2}(\frac{x}{\delta}) - \frac{1}{2}(\frac{x}{\delta})^3) & \text{if } -\delta \leq x \leq \delta \\ 1 & \text{if } x > \delta \end{cases}$$

The smoothness of the function and implicitly the thickness of the transition zones between the matrix and the collars, or the collars and the void are controlled by the length scale  $\delta$ . This is of interest from a physical point of view because they are not as abrupt as in conventional engineering structural parts. The stiffness of the void material (inside the lumen) has been chosen as 1% of the stiffness of the collar material and the length scale  $\delta$  as one half of the size of an element. Several verifications have been carried out to assess the accuracy of the approach by comparison with the classical one (explicit meshing of the structures) and have shown that the strain concentration tensor  $A$  is well adapted.

Then the accuracy of the computation of the equivalent moduli is controlled by an adaptive meshing based on the minimization of the error on the following quantity of interest for each given macroscopic strain  $E$ :

$$J(u_1) = \int_Y C : (\varepsilon_y(u_1) + E)$$

The so-called a-posteriori error estimation is driven by the Bangerth & Rannacher (2003) approach for this quantity which uses a Lagrangian formulation with an adjoint state. As explained there the error boils down to two residuals: one is associated with the equilibrium at the interface between the elements, and another one with the adjoint equilibrium. In general, a different refined mesh is produced for each quantity of interest. The figure below shows the obtained meshes after refinement for two different macro-extensions.



377

378

379

Figure 11, Left to right: Initial mesh used for equivalent moduli, Level 4 mesh for macro-extension along z-axis, Level 4 mesh for extension along x-axis

The computation of the maximum principal stress is much more stringent. The chosen quantity of interest is:

382

$$J(u_1) = \int_{Y_c} \sigma_{max}$$

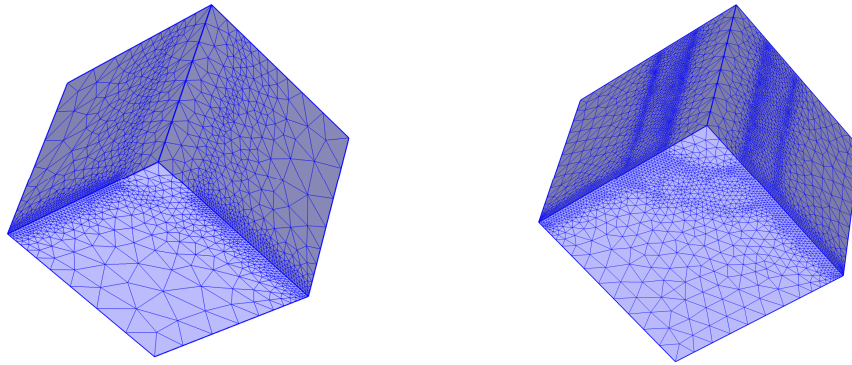
383

384

385

Again, the same approach proposed by Bangerth & Rannacher (2003), is used now with a quantity of interest that is no more linear with respect to the displacement. Nevertheless, the theory may be extended correspondingly.

386 With this particular choice the refinement process is most adequately operated inside  
 387 the collars and more precisely at the interface collars / void and close to the intersection PTD  
 388 / LBC. The Figure 12 shows an illustration of the proposed technique with 4 levels of  
 389 refinement.



390

391 *Figure 12 : Examples of meshes obtained for failure investigation with the following parameters  $\theta_0 = 0, \varphi_0 =$   
 392  $\frac{\pi}{4}$  (left) and  $\theta_0 = \frac{\pi}{2}, \varphi_0 = \frac{\pi}{4}$  (right)*

393 The technique has been validated by comparison with an analytical solution e.g.  
 394 cylindrical hole in a plate and has shown to provide the stress concentration factor with a  
 395 relative error of less than 0.1%.

396

#### 4.6. Investigated geometries and local properties

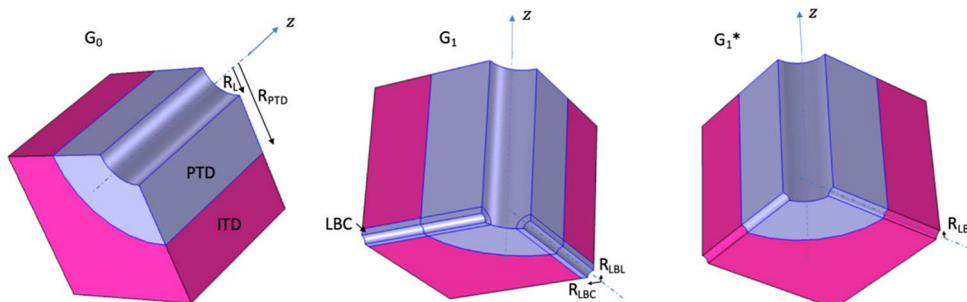
397 Our study is in two steps. A first step is dedicated to the validation of the implicit  
 398 modeling we propose and to a first assessment of the impact of the LB and their collars.  
 399 Here, the considered geometries are defined using data from the literature.

400 The second step consists in defining new geometries from our image analysis results  
 401 and assess the impact of LB and their collars on the stress concentrations depending on the  
 402 location in dentin and on the stress orientation.

403

404 In the first step, three geometries ( $G_0$ ,  $G_1$  and  $G_1^*$ ) are considered (Figure 13), mainly  
 405 to validate the implicit modeling:

- 406 •  $G_0$  is constituted of a tubule (L+PTD) surrounded by an ITD matrix
- 407 •  $G_1$  is constituted of  $G_0$  where four lateral branches (LBC for lateral branch lumen+ LBC)
- 408 with a collar are added
- 409 •  $G_1^*$  is constituted of  $G_0$  where four lateral branches without collar are added

410  
411

*Figure 13 : The first three considered geometries and their geometrical parameters*

412 Those geometries are illustrated in Figure 13 and their geometrical parameters values are  
 413 presented Table 1. They are defined using the data from the literature (Kinney *et al.* 1996).  
 414 The LB characteristics have been chosen in accordance to Mjör and Nordahl (1996). They  
 415 indeed estimated LB diameter to vary from 25nm to 700nm away from mantle dentin. As  
 416 there is no data available concerning the LBC, we hypothesized a ratio  $\mu_{LBC} = \frac{D_{LBC}}{D_{LBL}}$  of 0.5.

	L (lumen)	PTD	LBL	LBC	ITD
Diameter ( $\mu\text{m}$ )	1	3	0.2	0.4	-
E (GPa)	-	30	-	30	20

417 *Table 1 : Geometrical and local mechanical parameters for the three considered geometries (for a cubic cell of  $5\mu\text{m}$  side).*

418 For those three geometries the ratio of highly mineralized collars (LBC and PTD), intertubular  
 419 dentine (ITD) and porosity (LBL and L) are roughly the same: 25%, 72% and 3% representing  
 420 an area in middle dentin. The  $G_1$  geometry has been used to validate our implicit modeling  
 421 by comparing our results in terms of effective properties and stress concentration factor  
 422 with a more classical explicit approach (i.e. where the geometrical entities are meshed).  
 423 Then the role of the branches and their collars on the equivalent moduli and stress  
 424 concentration have been investigated.

425 Then, in the second step three other geometries with LBC are proposed mimicking the  
 426 three areas observed and quantified by SEM. And finally, the effect of the microstructure  
 427 orientation on stress concentration is assessed.

## 428 5. Results and discussion

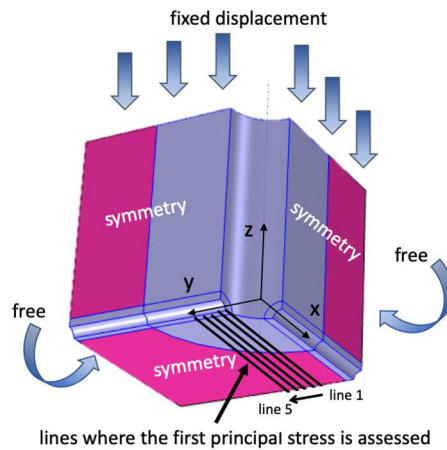
429 This section is divided in two subsections, the first one dedicated to the preliminary  
 430 geometries ( $G_0$ ,  $G_1$  and  $G_1^*$ ) and the second one to the image-based simplified geometries.

### 431 5.1. Preliminary study of the impact of LB on the mechanical 432 behavior of dentin (first step)

#### 433 *Implicit modeling validation*

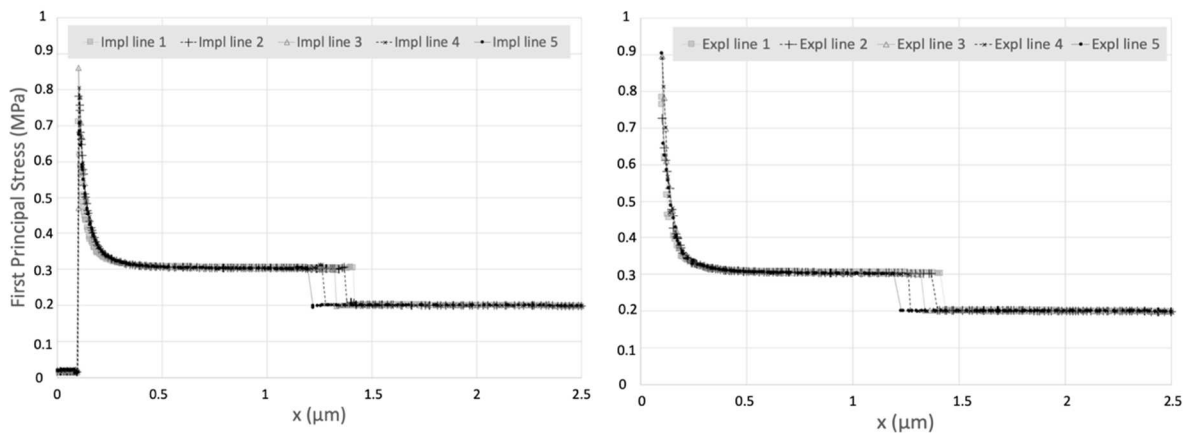
434 The use of the implicit modeling described in 4.5 is validated through the estimation of  
 435 the equivalent moduli for  $G_1$  with implicit modeling and explicit modeling (i.e. where the  
 436 microstructures are all meshed initially). The differences in equivalent elastic moduli, shear  
 437 moduli and Poisson ratios are less than 0.51%. The implicit modeling is thus validated for  
 438 those estimations.

439 A more sensitive assessment is the stress concentration. In order to validate the use of  
 440 the implicit modeling to probe stress concentration, we compare the first principal stress on  
 441 lines where the stress is intense in tension when the structure is loaded in z direction.  $G_1$   
 442 configuration with  $E_{PTD}=30\text{GPa}$  under tension (constrained displacement of 1% in z direction  
 443 on the upper face (Figure 14) is considered with the two types of modelling (explicit or  
 444 implicit).



445  
446  
447 *Figure 14 : Boundary conditions and location of lines where the first principal stress is assessed in the case of the proposed tensile test in direction z (for comparison Implicit/Explicit modeling)*

448 The first principal stress along chosen lines cutting the interface between LBL and LBC  
449 at right angle is assessed in both cases (implicit and explicit modeling) and the maximum  
450 stress in the whole volume is recorded. The two modeling approaches provide very similar  
451 first principal stress values (Figure 15) with a higher estimation of the maximal first principal  
452 stress value found in the explicit modeling approach (0.90 MPa on line 3). The maximum first  
453 principal stress within the solid part of dentin (i.e. either in PTD or in ITD) is 0.94 MPa and  
454 0.90 MPa respectively in explicit and implicit modeling. We argue that the implicit modeling  
455 results are satisfactory and in the next sections, the implicit modeling approach is used.  
456



457  
458 *Figure 15 : First principal stress assessment along the chosen lines with both modeling approach.*

459 Furthermore, from a physical standpoint, the explicit computation enhances corner  
460 and interface singularities with artificial curvature discontinuities issued from the Computer  
461 Aided Design (CAD) output and zero thickness interface while they are much smoother in  
462 reality. For all these reasons the implicit computation is preferred and used in the sequel.

#### 463 *Impact of LB on homogenised moduli*

464 The three geometries presented in Figure 13 are investigated. The results in terms of  
465 equivalent moduli are presented in Table 2.

466  
467  
468

	$G_0$	$G_1$	$G_1^*$
$E_x$ (GPa)	20.5	20.6	20.5
$E_z$ (GPa)	21.8	21.7	21.7
$\nu_{xy}$ (-)	0.30	0.30	0.30
$\nu_{xz}$ (-)	0.28	0.28	0.28
$G_{xy}$ (GPa)	15.7	15.7	15.7
$G_{xz}$ (GPa)	16.1	16.1	16.0

Table 2 : Equivalent stiffness matrix parameters for  $G_0$ ,  $G_1$  and  $G_1^*$  configurations ( $E_{PTD}=30GPa$ )

469

470 As reported by Qin and Swain 2004, the modulus parallel to the tubule (here,  $E_z$  equal  
471 to roughly 21.7 GPa) is higher than the modulus perpendicular to the tubule (here,  $E_x$  equal  
472 to roughly 20.5GPa). Bar-on *et al.* 2012 found the opposite which can be explained by the  
473 fact that the anisotropic fibrillar structure of ITD has been taken into account in their study.

474

475 We can define and estimate  $E_{VOIGT}$ , the upper limit of the equivalent moduli:

476

$$E_{VOIGT} = c_{PTD}E_{PTD} + c_{ITD}E_{ITD} + c_L E_L$$

477

$$E_{VOIGT} = 21.9GPa$$

478

479 With  $c_{PTD}$ ,  $c_{ITD}$ ,  $c_L$  the volume ratios of PTD, ITD and L and  $E_{PTD}$ ,  $E_{ITD}$  and  $E_L$  their  
480 local modulus ( $E_L = 0GPa$ )

481

482  $E_{VOIGT}$  is roughly the same for the 3 configurations ( $G_0$ ,  $G_1$  and  $G_1^*$ ) since the ratios  
483 differs only slightly.  $E_{VOIGT}$  is known to be a good approximation in the direction parallel to  
484 the major axis of inclusions so it can be compared to  $E_z$  (in the direction parallel to the  
485 tubule) and we remark that  $E_z$  is very close to  $E_{VOIGT}$ , although it remains lower.

484

485 We can also define and assess  $E_{REUSS}$ :

486

$$E_{REUSS} = \frac{1}{\frac{c_{PTD}}{E_{PTD}} + \frac{c_{ITD}}{E_{ITD}} + \frac{c_L}{E_L}}$$

487

488  $E_{REUSS}$  is known to be a good approximation in the direction perpendicular to the  
489 major axis of inclusions so it can be compared to  $E_x$  (in the direction parallel to the tubule).  
490 But  $E_{REUSS}$  almost vanishes here because of the modulus  $E_L = 10^{-2}GPa$ . However, to get  
491 non-vanishing modulus, we choose to define:

491

$$E_{REUSS}^* = \frac{1}{\frac{c_{PTD} + c_L}{c_{PTD}E_{PTD}} + \frac{c_{ITD}}{E_{ITD}}}$$

492

$$E_{REUSS}^* = 13.62GPa$$

493

494 As for  $E_{VOIGT}$ ,  $E_{REUSS}^*$  is roughly the same for the three configurations. The value found  
495 is not corresponding to  $E_x$  so Reuss estimation does no manage to model the behavior of the  
496 material in the direction parallel to the tubule.

496

497 Poisson's ratios are roughly the same and close to 0.3. Nevertheless, the value of  $\nu_{xz}$  is  
498 slightly lower than  $\nu_{xy}$ . This can be explained by the fact the stiffer tubule is affecting  
499 (lowering) the expansion parallel to it (direction z) when a loading is applied perpendicular  
500 to the tubule (direction x). The values of  $\nu_{zx}$  are not affected.

500

501 The shear moduli  $G_{xz}$  are slightly higher than the shear moduli  $G_{xy}$  (for all the  
502 configurations), the impact of the rigid tubule is indeed more important with a xz (or yz)  
503 shear. Even though it is difficult to compare so close values, we can notice that the shear

503 modulus  $G_{xy}$  is higher when lateral branches with a mineralized collar are present and the  
 504 lowest value is obtained when there are lateral branches with no collar.

505 The experimental data are giving a wide range of values for dentin Young's modulus as  
 506 it was pointed out by Kinney et al. [Kinney2003]. With the proposed calculations, we  
 507 investigate an intermediate scale not probed by experiments (experiments are mainly on  
 508 millimetric samples or are probing local properties with nano-indentation) so it is difficult to  
 509 compare our results with finesse to experimental results. However, we can see that the  
 510 variation with respect to the orientation of tubule is in accordance with Lees and Rollins  
 511 [Lees&Rollins1972] but in contradiction with Kinney et al. [Kinney2002]. The organization at  
 512 the scale below has to be taken into account to further investigate this point

513 The main finding of this preliminary study is that the equivalent moduli seems only  
 514 slightly impacted by the presence of LB.

### 515 *First insight on the impact of LB on stress concentration*

516 We loaded the three configurations ( $G_0$ ,  $G_1$  and  $G_1^*$ ) as illustrated Figure 14. So here, only  
 517 one cell is considered contrarily to the next image-based study where a cell is considered  
 518 among an infinity of other cells (following the concept of periodic cell).

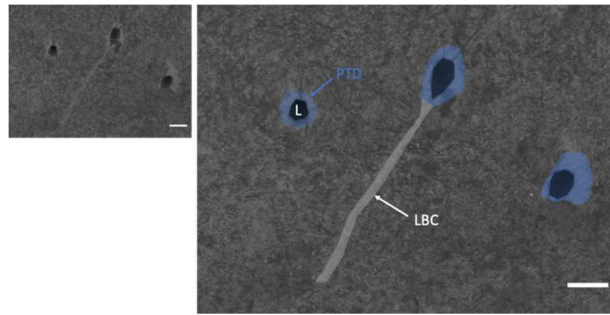
519 In this preliminary study of the LB impact, we found that the impact of LB is non negligible,  
 520 the maximum principal stress rises to reach 3 in  $G_1$  and  $G_1^*$  whereas there is no stress  
 521 concentration in  $G_0$  in this mechanical load configuration (directed along the tubule axis).  
 522 This shows that the impact of LB is to be taken into account.

523 In the second step of our study, we propose to do so using periodic cells mimicking three  
 524 areas in dentin. Those three areas will be defined using the results of our image analysis  
 525 protocol on dentin SEM images at different locations. The periodicity will allow to consider  
 526 that the cell is surrounded by other identical cells, enabling to take into account cell  
 527 interactions. The load will also be considered with different directions because as the tubule  
 528 orientation is varying in dentin, the periodic cell is in reality loaded not only along the tubule  
 529 axis.

## 530 **5.2. Stress concentration in the tissue with a geometry** 531 **deduced from SEM image analysis**

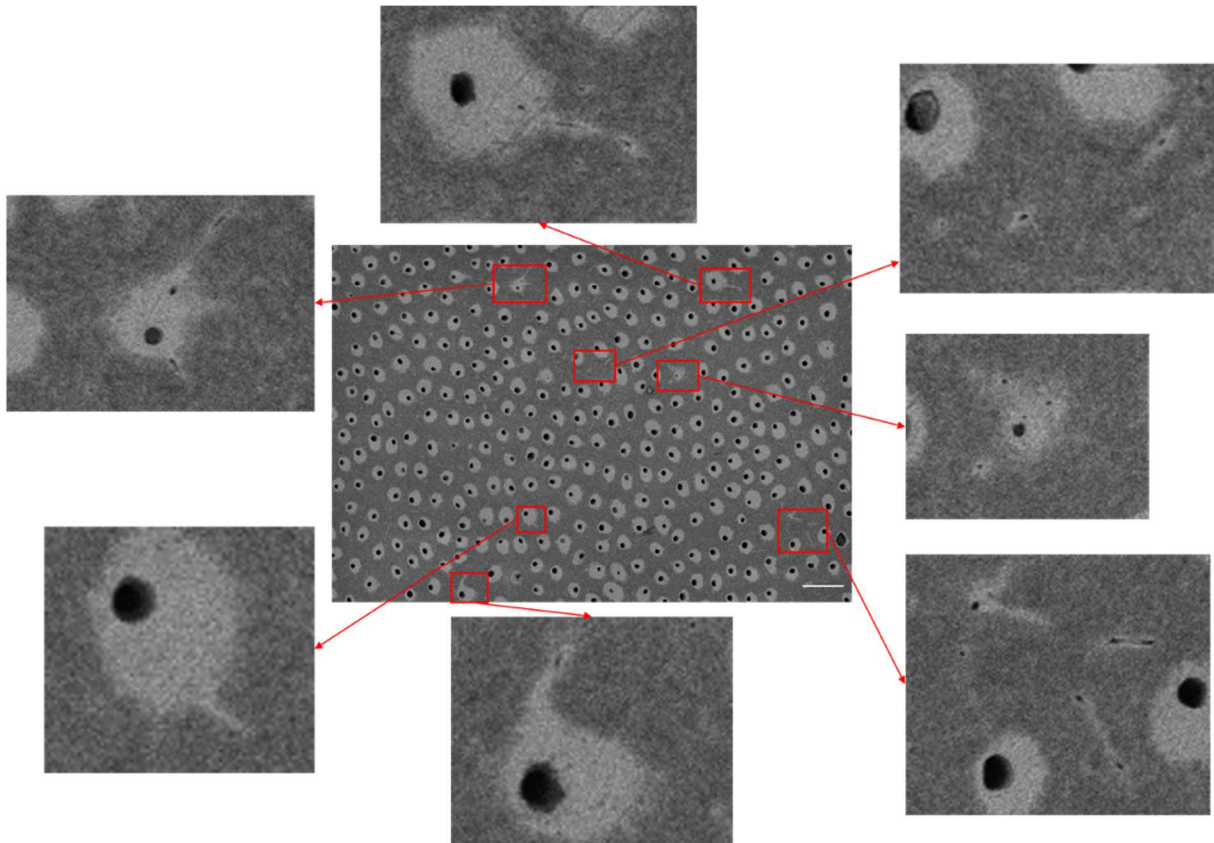
### 532 *SEM Image Analysis*

533 An illustrative SEM image showing the investigated geometrical entities is presented in  
 534 Figure 16. On this SEM image, we can clearly observe a quasi linear dense area prolongating  
 535 the PTD of the second tubule. We can assume that the corresponding lateral branch is  
 536 composed of a highly mineralized collar (LBC) and a lumen (LBL), the lumen is probably  
 537 located below or above the cutting plan. As the LBC is statistically not cut in its middle plan,  
 538 the LBC diameter measurement on that type of 2D image provides an underestimated value  
 539 for its diameter. In our model (detailed in section 4), the same stiffness is affected to the  
 540 dense areas corresponding to LBC and PTD, an hypothesis supported by the finding of  
 541 Zanette et al. (2015). The texture of ITD is due to its mineral/organic composite composition  
 542 at the nanoscale.



543  
544  
545

Figure 16 : Example of a dense lateral collar perpendicular to a tubule observed by SEM in BSE mode. L=tubule lumen; PTD=Peritubular dentin LBC=Lateral branch collar. Scale bar : 2μm.



546  
547

Figure 17: Examples of LB observed by SEM in BSE mode. Scale bar: 10μm

548 On a second SEM image, different configurations of LB arising from tubules are  
549 highlighted (Figure 17). Using this image, a first approximation of the ratio  $\mu_{LBL}$  is calculated:

550 
$$\mu_{LBL} = \frac{D_{LBL}}{D_{LBC}} \cong 0.3$$

551 This ratio will be used to deduce  $D_{LBL}$  from the lower resolution image used for the  
552 analysis. Lower resolution images have been used in order to have wider and so more  
553 representative areas to analyze.

554 Depending on the location, the density and diameter of LBC (and so LB) vary. So, after  
555 the qualitative analysis of a few high-resolution SEM images, a quantitative analysis is led on  
556 the dentin constituents. The results concerning L, PTD and ITD ratios, dimensions and tubule  
557 density (equivalent to L density) are summarized in Table 2.

Location	L (%area)	Mineralized part (%area)	ITD (%area)	L diameter $D_L$ (μm) (SD)	PTD diameter $D_{PTD}$ (μm) (SD)	L density (/mm <sup>2</sup> )
E	0.9	8.5	90.6	0.82 (0.16)	1.82 (0.27)	17685

<b>M</b>	4.7	13.9	81.4	1.38 (0.20)	2.30 (0.33)	30229
<b>P</b>	12.5	29.0	58.5	1.52 (0.19)	2.21 (0.32)	69168

558

Table 3 : Distribution of area fraction, diameter and density of the dentin constituents

559

The detected porosity is only due to tubules' lumen L. Indeed, the LB are mostly cut parallel to their axis making it more likely to reveal their collar (LBC). The porosity values between 0.9 and 12.5 % are in the range of the values found in the literature: a global porosity of 4% (mean value over massive samples obtained by mercury intrusion porosimetry) was reported in Vennat et al. (2009) and a local porosity near DEJ of 1.2% was reported by Vennat et al. (2017).

565

The lumen diameter increases continuously from DEJ to deep dentin, whereas the size of the peritubular collar first increases and then remains quasi-constant from M (middle dentin) to P (deep dentin). The tubule density (L density) is within the range found in the literature (Garberoglio & Brännström 1976, Pashley et al. 1989). The mineralized part takes into account both PTD and LBC. A special attention is paid to their diameter distribution (Figure 18). The count (%) corresponds to the number of entities which have this range of diameter over the total number of entities. This does not take into account the surface ratio of the entities. The distribution is clearly bimodal as it is for the porosity (Vennat et al. 2017).

566

567

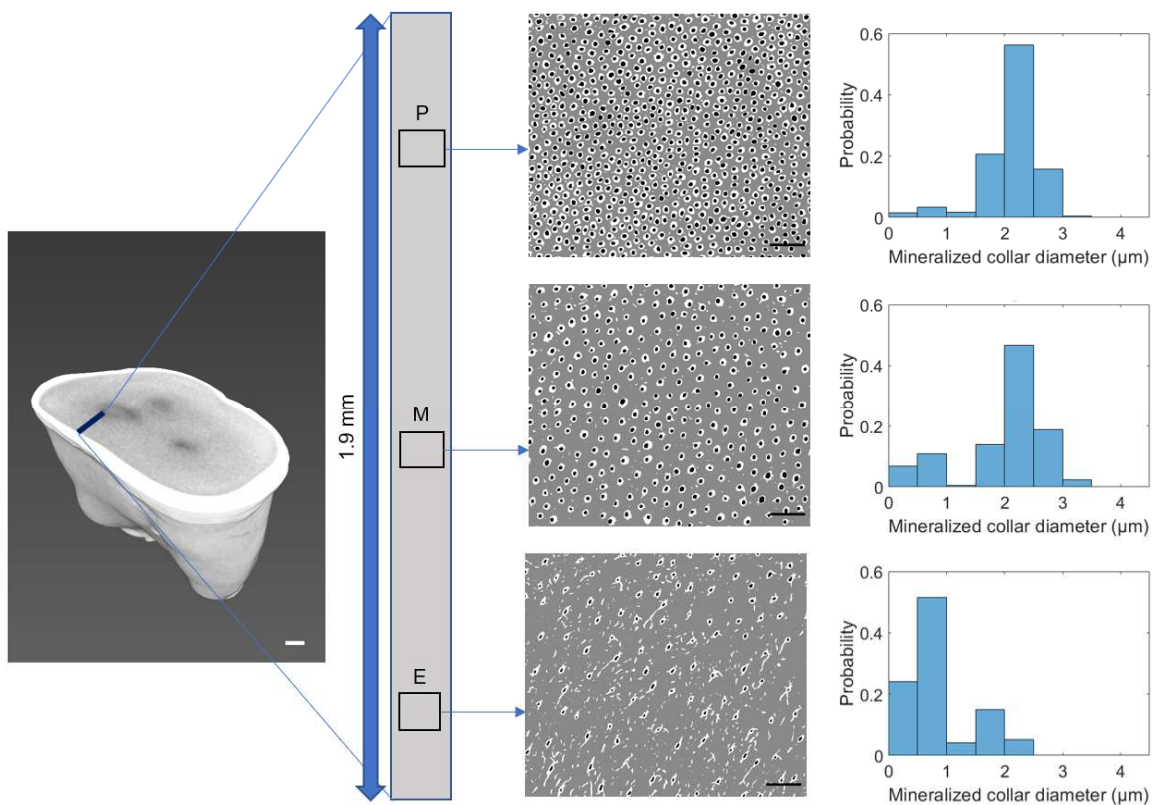
568

569

570

571

572



573

574

Figure 18: Mineralized entities diameter depending on location. White scale bar: 1mm. Black scale bars : 15µm

575

The mean values of LBC ratio (% area) and diameter are summarized in Table 4.

576

Location	%area of LBC (%)	$D_{LBC}$ (µm)(SD)
<b>E</b>	2.65	0.61 (0.18)

<b>M</b>	0.33	0.57 (0.15)
<b>P</b>	0.13	0.58 (0.14)

577

Table 4. Quantification of lateral branches collars LBC

578 There is no significant difference between lateral branch collar diameter data from  
 579 deep, middle and superficial dentin. Mjör & Nordahl (1996) have described the LB  
 580 morphologies in dentin but their possible mineralized collar has never been discussed. So  
 581 our quantification is used as a basis for defining the geometry of dentin microstructure in  
 582 the proposed model. Three areas (E, M and P) are defined with the following parameters to  
 583 mimic the constituents ratios, diameters and  $\mu_{LBL}$  (Table 5):

584

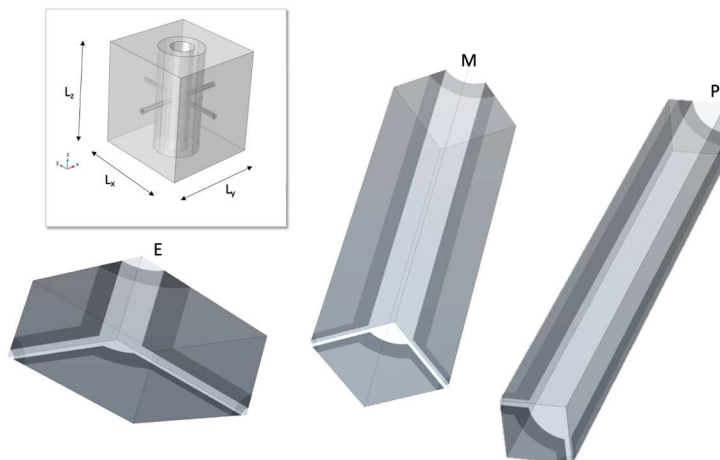
Area	E	M	P
<b>D<sub>L</sub></b> ( $\mu\text{m}$ )	0.52	1.22	2
<b>D<sub>PTD</sub></b> ( $\mu\text{m}$ )	1.04	2.38	3.6
<b>D<sub>LBL</sub></b> ( $\mu\text{m}$ )	0.20	0.20	0.20
<b>D<sub>LBC</sub></b> ( $\mu\text{m}$ )	0.60	0.60	0.60
<b>L<sub>z</sub></b> ( $\mu\text{m}$ )	2.40	15.07	22.26
<b>L<sub>x</sub>=L<sub>y</sub></b> ( $\mu\text{m}$ )	4.94	4.43	2.65

585

586

Table 5 : The geometrical parameters of the three image driven periodic cell geometries.  $L_z$  and  $L_x=L_y$  are the lengths of the cell along the tubule and perpendicular to the tubule respectively.

587 The three periodic cells corresponding to the three considered areas are represented  
 588 Figure 19.



589

590

Figure 19: the three image-based configurations (E, M and P)

591 Here, the SEM image analysis results constitute a first set of data that is used as an  
 592 input for the proposed model. Further studies should be led to confirm this study and enrich  
 593 it with data on other types of teeth or donor age.

#### 594 Variations of the equivalent stiffness from pulp to enamel

595 To be the closest to a complex real microstructure, the implicit modeling presented in  
 596 section 4 is chosen because it allows to do "image-driven" modeling easily. As imaging  
 597 techniques are more and more powerful, it is attractive to design a modeling method that  
 598 can be applied to those images quasi-directly. In our study, the 2D SEM images constitute a  
 599 basis to define a simplified geometry but further study could use 3D images stack directly.

600 With the parameters corresponding to the three areas defined in Table 5, we evaluate the  
 601 orthotropic parameters of dentin depending on the location (Table 6).  
 602

	<b>E</b>	<b>M</b>	<b>P</b>
$E_z$	20.4	19.8	17.7
$E_x=E_y$	19.7	17.5	12.4
$\nu_{xy}$	0.30	0.29	0.22
$\nu_{xz}$	0.29	0.27	0.21
$G_{xy}$	15.1	13.0	6.6
$G_{xz}$	15.3	14.1	10.5

603 *Table 6 : Equivalent stiffness matrix parameters identified for E, M and P configurations*

604 The modulus in the tubule direction,  $E_z$ , does not vary drastically within depth: the void  
 605 of the lumen is balancing the rigidity of the collar. The modulus in the direction  
 606 perpendicular to the tubule,  $E_x$ , is lower than  $E_z$  for the three locations which is in  
 607 accordance with Qin & Swain (2004). When taking into account the lower scale organization,  
 608 Bar-On *et al.* (2012) showed that it is possible to have  $E_z$  smaller or equal to  $E_x$ , highlighting  
 609 the role of the lower scale in the global mechanical behavior of dentin but the impact of LB  
 610 was not taken into account.

611 We find out that near enamel (configuration E) the behavior is quasi-isotropic.  
 612 However, this effect could be counterbalanced by the collagen fibril orientation effect which  
 613 is not taken into account in the proposed study. Further study could also investigate the role  
 614 of the angle with which the LB is rising from the tubule.

615 From E to P, the anisotropy is enhanced to reach the P configuration which can be  
 616 compared to a unidirectional fiber composite with  $E_z$ , the modulus along the fibers, very  
 617 close to Voigt modulus  $E_{VOIGT}$  and  $E_x$ , the modulus perpendicular to the fibers, very close to  
 618 Reuss modulus  $E_{REUSS}^*$ . The same trend is observed for the shear moduli.

619 The poisson's ratios  $\nu_{xy}$  and  $\nu_{xz}$  decrease from E to P in accordance with the increase  
 620 in terms of porosity.

### 621 *Failure criterion*

622 In this last section, a micromechanical failure criterion in the dentin cell microstructure  
 623 is presented. It is well known that in composite materials, apart from simple cases, the  
 624 failure criterion cannot be extracted solely from the macro-stress calculated from the  
 625 homogenized moduli (Christensen 2013).

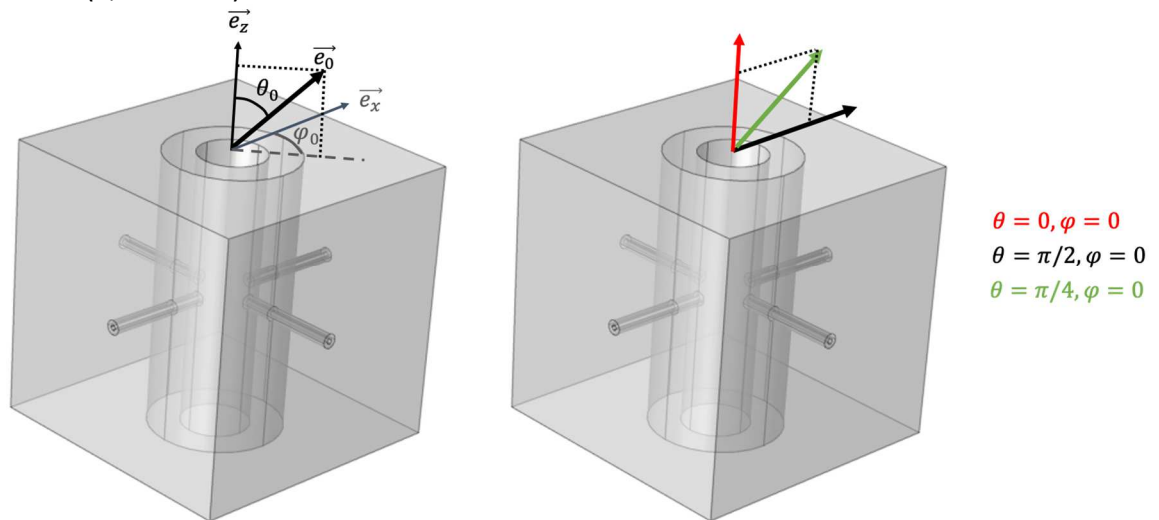
626 Typically, in our case, the failure initiation may result from overstress in the collars  
 627 either at the interface with the lumen or at the intersection of the collars or at the interface  
 628 between the matrix and the collar, inside the matrix.

629 We show underneath that depending on the stress state these stress concentrations  
 630 may justly occur at these different locations. This means from a macroscopic viewpoint, the  
 631 failure criterion may be considered as a multi-mechanism, i.e. with a set of inequalities, in  
 632 the sense referenced by Mandel (1965).

633 For illustration purpose, here, we limit ourselves to the special case of a uniform  
 634 uniaxial macroscopic traction applied on the orthotropic homogenized material in a  
 635 direction which is not necessarily the one of the orthotropic axes. This direction is defined by  
 636 two angles:  $\theta_0$  the angle of the traction with the tubular channel axis, and  $\varphi_0$  the angle with  
 637 the lateral branch x-axis (Figure 20). It is important to consider this general case because

638 during the chewing process the orientation of the principal stress with respect to the  
 639 channels orientation inside the dentin material varies a lot from the pulp to the enamel. It  
 640 has been underlined in the literature (Pilkey & Pilkey, 2008) that finite width, material  
 641 orthotropy, multiple holes, hole intersections are parameters increasing the concentration  
 642 factors, so that we want to explore these features in our particular case. Stress repartition in  
 643 geometries made of tubes with cylindrical holes have been investigated by various authors  
 644 (Pilkey & Pilkey 2008, Wu 2003) but the loading is in most cases an internal pressure and the  
 645 tube is very thin in coherence with the dedicated applications (pipes with some fluid inside).  
 646 In Wu (2003), a tube with a cylindrical hole is considered and a tensile loading is considered.  
 647 A stress concentration factor of 3 to 8 is found depending on the geometry. It is not possible  
 648 to directly compare those value to our results since the considered geometry is not the  
 649 same, but we can notice that the stress concentration factor can be sensibly higher than 3.

650 In the next paragraphs, we simply comment a few particular cases of macro-traction  
 651 underlining the micro-mechanism sources of failure (Figure 20) in three geometrical  
 652 configurations (E, M and P).



653  
 654 *Figure 20 The considered loading cases of macro-traction*

655 **The case ( $\theta_0 = 0, \varphi_0 = 0$ )**

656 The macro-traction is along the tubular channel. If no LB is considered, the stress is  
 657 quasi-uniform in each geometrical entity and K is roughly 1. Whereas in the configurations  
 658 where the LB are taken into account this overstress ratio grows to 3 to 4 in the E, M or P  
 659 configurations (Figure 21).

660

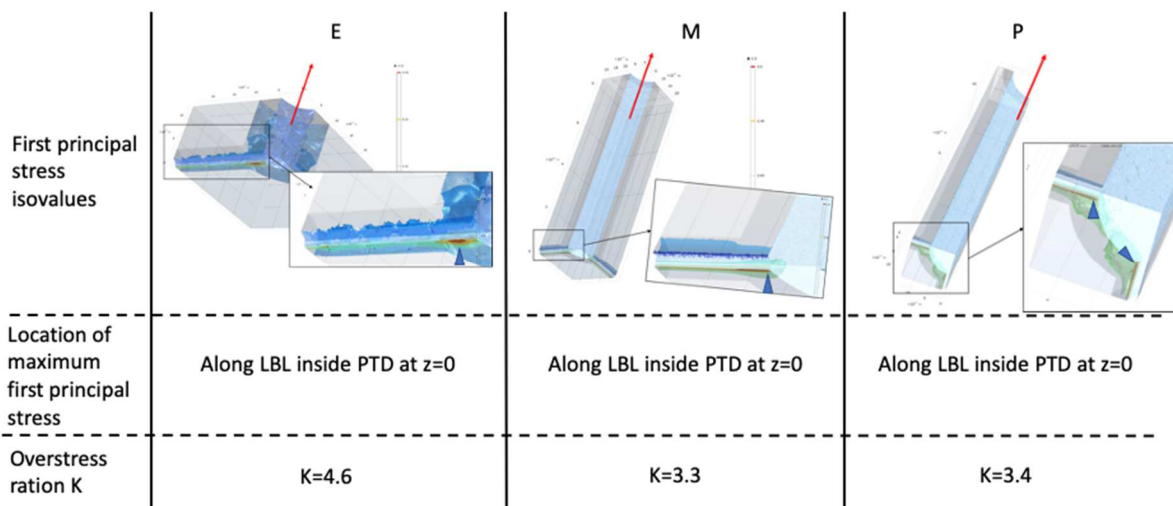


Figure 21 The considered cases with LB for  $\theta_0 = 0, \varphi_0 = 0$  and the corresponding stress concentration location (blue arrow heads) and overstress ratio.

661  
662  
663

664 The maximum stress concentration occurs in a mild singular location with respect to  
665 the tubule-branches intersection. Its value of roughly 3 in M and P configurations  
666 corresponds the classical value obtained for a plate with a hole loaded with an axial traction  
667 far from the hole.

668 With the higher density of LB (configuration E), the overstress ratio reaches a factor of 4.6,  
669 which is the order of magnitude found due to orthotropy (Pilkey & Pilkey, 2008). In E  
670 configuration, due to cell periodicity, LB are the closest so the stress concentration may rise  
671 in between those holes (Pilkey, 2005).

672

673 In all the considered configurations, we see here that the main contribution to the  
674 failure is a hoop stress increase in the tubule collar PTD at the boundary with the lateral  
675 branch lumen. As seen in section 5.1, the stress concentration reaches the same level in a  
676 configuration without or with LBC. But the collars (PTD and LBC), when they are present,  
677 seem to withstand the highest levels of stress (figure 22) thus acting as a helmet for ITD.  
678 Those collars may thus crack but we can infer that the mineralization process due to aging  
679 (PTD is growing through life) is in fact a repair process.

680

681 For M and P configurations, the generated level of overstress can be obtained with a  
682 tubule only loaded perpendicular to its axis (classical overstress ratio of 3). In the next  
683 paragraph, a more harmful case is considered where the stress concentrations of the two  
684 perpendicular arrays of channels are interacting.

684

685

686

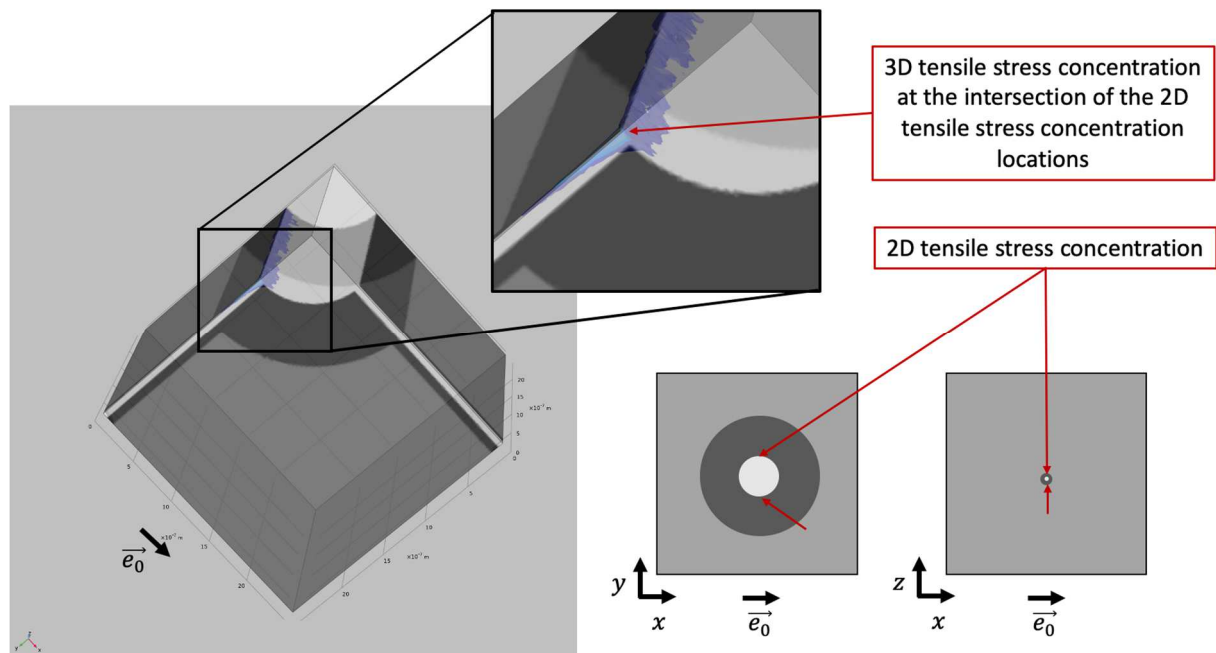
687 **The case ( $\theta_0 = \frac{\pi}{2}, \varphi_0 = 0$ )**

688 The macro-traction is along the lateral branch oriented in the x-direction.

689 If only the tubule is present, the overstress is occurring all along the boundary of the  
 690 tubule with its lumen and the overstress ratio is 3. If only the lateral branches are present,  
 691 the overstress may occur all along a line at the boundary of the branch oriented in the y-  
 692 direction and its lumen and the overstress ratio is 3. In the case where both are present, the  
 693 overstress appears along a line at the intersection between the tubule lumen and the LBL  
 694 which provides a corner singularity at a highly loaded location (Figure 22). Consequently, the  
 695 concentration factor is very localized and much higher than in the case ( $\theta_0 = 0, \varphi_0 = 0$ ) to  
 696 reach a maximal value of K between 7 and 8 in the different configurations. The highest  
 697 value of K is obtained in P configuration which may be due to the interaction between  
 698 neighboring cells as the maximum stresses are obtained at the interface with the lumen and  
 699 because the tubules are, in this area, close to each other. Due account between adjacent  
 700 cells, is an interesting ability of the periodic assumptions.

701 We argue that this case is the most harmful case because it is arising from the  
 702 interaction of the stress concentration of the two types of channels (that can be seen as a  
 703 constructive interference). The drastic rise of overstress (superior to 7) due to the presence  
 704 of LB is indicating that the impact of LB has to be taken into account when considering  
 705 dentin failure.

706



707  
708

Figure 22 : Illustration of the stress concentration location at the intersection of dentin channels

709 **The case ( $\theta_0 = \frac{\pi}{4}, \varphi_0 = 0$ )**

710 This is still a more complex state of stress which is interesting to decompose along the  
 711 symmetry axes for comparison purpose with the two preceding cases:

$$712 \quad \sigma = \frac{\sigma_0}{2} (i_x \otimes i_x + i_z \otimes i_z + i_x \otimes i_z + i_z \otimes i_x)$$

713

714 This is a combination of the first two states of stress, case  $(\theta_0 = \frac{\pi}{2}, \varphi_0 = 0)$  and case  
 715  $(\theta_0 = 0, \varphi_0 = 0)$ , augmented by a transverse shear which should transfer some additional  
 716 stress to the tubule interface with the lumen.

717 Because of the xx-component of the stress field, the overstress occurs all along the  
 718 boundary of the tubule with its lumen. The zz-component of the stress field, which should  
 719 imply a stress concentration at the interface between the LB and its lumen at the bottom of  
 720 the considered cube, seems to have a less harmful effect. The lines corresponding to the  
 721 maximum stresses due to zz-component and the xx-component of the stress field have, in  
 722 this case, no intersection in the solid. Nevertheless, this is a branch-tubule intersection (a  
 723 geometrical singularity) that provides the maximum overstress localization with a factor  
 724 varying from 3.5 to 5 in the different configurations.

725 The computed maximum overstress is one more time located at the intersection of the  
 726 tubule lumen and the lateral branch lumen while the overstress spreads along a line at the  
 727 intersection of the tubule with its lumen.

728

<b>K</b>	$(\theta_0 = 0, \varphi_0 = 0)$	$(\theta_0 = \frac{\pi}{2}, \varphi_0 = 0)$	$(\theta_0 = \frac{\pi}{4}, \varphi_0 = 0)$
<b>E</b>	4.0	7	4
<b>M</b>	3.3	6.9	5.2
<b>P</b>	3.4	5.2	7.2

729

Table 7

730 Other cases of  $(\theta_0, \varphi_0)$  couples have been considered but the overstress was lower  
 731 than in the cases just presented above. Table 7 sums up the overstress ratio variation within  
 732 depth and depending on the load orientation for the proposed cases.

733

734 In brief, the maximum overstress ratio reaches 7 when the periodic cell is loaded in xx  
 735 or yy-direction i.e. along a LB. It leads indeed to constructive interaction of stress  
 736 concentration due to the yy (or xx-LB respectively) and due to tubule.

737 Periodicity enhances stress concentration. When the location of stress concentration  
 738 is close to the cell boundary, we find a higher value of K :

739

- for E when loaded in zz-direction (interaction due to LB)
- for P when loaded in xx or yy-direction (interaction due to tubules)

740

741 The collars (PTD and LBC) seem to concentrate the higher stress levels acting as a  
 742 protective shield for the ITD. The mineralization process of the dentin (PTD layer is growing  
 743 during life) would hence be the repair process of the dentin if a crack has been formed.

744

745 In summary, the study of a macroscopic traction applied to the material with various  
 746 orientations with respect to the symmetry axes has shown several features. An overstress of  
 747 about 4 is obtained when the traction is aligned with the tubule but may grow to twice this  
 748 ratio when the traction is aligned with one of the lateral branches which differs with the  
 749 classical plate with a hole where the size of the hole does not matter. The highest factor is  
 750 located at the intersection between the branches and the tubule with the constructive  
 751 interference of both lumens-induced stress concentration. If we assume only a slight  
 752 heterogeneity ( $E_{PTD}=30\text{GPa}$  and  $E_{ITD}=20\text{GPa}$ ), a simple macroscopic failure criterion may be  
 753 proposed when either of the two following thresholds is violated,  $e_{LB}$ ,  $e_T$  and  $\sigma_{tmax}$   
 754 respectively the unit vectors giving the direction of the lateral branches and tubules and the  
 755 collar material strength under traction:  
 756

$$757 \left\{ \begin{array}{l} (\sigma(e_{LB}), e_{LB}) \leq \frac{\sigma_{tmax}}{K_{LB}} \\ (\sigma(e_T), e_T) \leq \frac{\sigma_{tmax}}{K_T} \end{array} \right.$$

758  
 759 With  $\sigma_{tmax}$  maximum tensile stress,  $K_{LB}$  and  $K_T$  the concentration factors described  
 760 above, i.e. of the order of 8 and 4 to give an order of magnitude. Because of the special  
 761 arrangement of the dentin microstructures, two physical different failure mechanisms  
 762 according to whether the traction direction is close to either to the tubule or lateral  
 763 branches directions exist and are taken into account in the proposed criterion. A safe and  
 764 simplified approach could be to account only for the maximum of both criteria but could  
 765 lead to a kind of conservatism design because during chewing the principal stress direction  
 766 with respect to tubule and lateral branches directions varies a lot. We think that the two  
 767 proposed inequalities embody and quantify rather well the two discovered overstress  
 768 mechanisms rather well.

769 Obviously additional inequalities could be introduced but it is believed that these two  
 770 criteria summarize in a simplified manner the investigations above. Post failure  
 771 considerations can obviously be proposed but are clearly outside of the scope of the present  
 772 study.

773 Here a SEM image analysis has been carried out and has led us to design simplified  
 774 geometrical configurations. Based on these configurations, a mechanical model has been  
 775 build and the behavior of the tissue has been studied depending on the modeled area (near  
 776 enamel, in middle dentin or near the pulp). The assumption of a periodic microstructure has  
 777 been made. Even if the dentin microstructure is a biological microstructure (so it is not  
 778 perfectly periodic as assumed here), we argue that this model is relevant as pointed out by  
 779 Kinney et al. [Kinney2001] in their study about spatial arrangement of tubules. Another  
 780 simplification has been made concerning the LB: the LB angle with tubule has been fixed to  
 781  $90^\circ$  but in reality it can be smaller in some areas. Further study could investigate inclined LB.  
 782 The PTD Young's modulus that has been fixed to 30GPa and this value is perhaps an  
 783 underestimation so further study could investigate the effect of a higher modulus.

784 Further studies could be conducted using directly 3D images acquired by 3D imaging  
 785 techniques such as plasma FIB-SEM for example. This is made possible by the use of the  
 786 implicit modeling proposed in this article. These studies would allow to take into account the  
 787 truly complex morphology of the dentin microstructure and, for example, to probe the

788 microstructure gradients within the depth of dentin, the non-alignment of the lumen and  
789 the peritubular collar axis, the S-curvature of tubules, the arched shape of LB, the  
790 collagen/minerals entanglement (that can be given by TEM imaging). It would also be  
791 interesting to quantify the impact of aging on LB microstructure for collar size should  
792 increase with age, as the tubule collar does. In dental practice, knowledge of potential  
793 fracture locations in dentin allows for adaptation to the potential restoration  
794 geometry/properties and a reinforcement of the tissue to prevent tooth failure if needed.  
795 Moreover, using this implicit modeling, any other phase (a fluid infiltrating or flowing in the  
796 pores, a resin that reinforces the structure...) can be easily added. So, this model can be  
797 easily enriched to become a poromechanics model that can be helpful in understanding the  
798 mechanical behavior of tooth but also the impact of flow or temperature changes within the  
799 tubules. Moreover, using this implicit modeling, any other phase (a fluid infiltrating or  
800 flowing in the pores, a resin that reinforces the structure...) can be easily added. So, this  
801 model can be easily enriched to become a poromechanics model that can be helpful in  
802 understanding the mechanical behavior of tooth but also the impact of flow or temperature  
803 changes within the tubules.  
804 A global picture of the mechanical behavior of the tooth can also be forseen. Too few studies  
805 are trying to understand how damage interacts with the intact tooth. The philosophy of the  
806 proposed tissue-scale study can be enlarged to a whole tooth where the dental tissues  
807 morphologies and properties gradient are taken into account.

808

809

## 6. Conclusion

810

811

812

813

814

815

816

817

818

819

820

821

822

823

824

825

826

827

828

829

830

831

832

In this paper, we focus on the impact of lateral branches on the equivalent stiffness and failure initiation in dentin. An implicit finite element analysis is proposed, where the geometry is not explicitly meshed but taken into account using level set functions and adaptative meshing.

We first validate this implicit modeling by comparing our results with a more classical explicit approach. We then show, on a cell corresponding to middle dentin, defined from the data available in the literature, that the lateral branches present in dentin do not influence the effective stiffness of the tissue. The lateral branches do, however, play a crucial role in stress concentration which will further initiate failure. Data on local characteristics are needed to investigate the role of these lateral branches depending on their location in dentin.

As a second step, SEM imaging is performed to quantify the lateral branches' characteristics (surface ratio, lumen and collar diameter) for different locations in dentin. An image-based simplified model is then built for three locations: near enamel (E), in middle dentin (M) and near the pulp (P). The effective stiffness is assessed and varies slightly from enamel to the pulp but the presence of LB is not an influencing factor as it was suggested by our preliminary results.

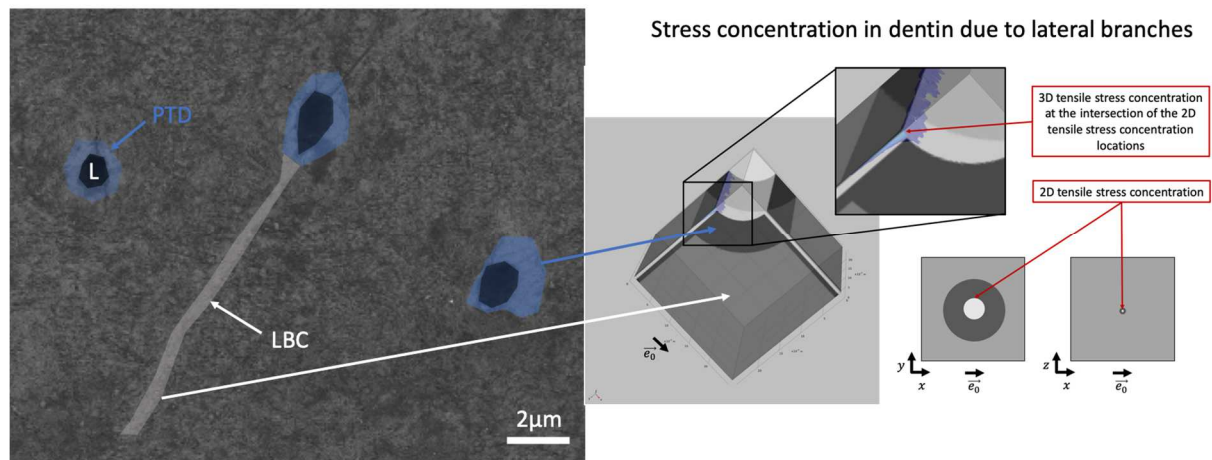
An original mechanical study is finally led on three defined configurations. A uniform uniaxial macroscopic traction is applied on the orthotropic homogenized tissue oriented in different directions. The stress concentration due to the presence of lateral branches can interact with stress concentration due to the presence of tubules leading to dramatic overstress ratios that would further initiate material failure. It is also shown that depending on the location those ratios are modulated: in E configuration, the impact of LB is higher

833 whereas in P configuration the impact of tubule lumens is higher due to the cell geometry  
834 and the periodicity.

835 As we know that not only the microstructure but also the nanostructure of dentin has  
836 a role to play in the mechanical behavior of dentin, an interesting perspective of this work is  
837 to add information concerning the nanoscale in the model. The “image-driven” model  
838 concept with the same implicit modeling approach could indeed be used with TEM imaging  
839 for example for modeling the entanglement of collagen fibrils and hydroxyapatite crystals in  
840 the tissue.

## 841 7. Graphical abstract

842



843

844

---

### 845 Acknowledgment

846 This work benefited from the financial support of the LabEx LaSIPS (ANR-10-LABX-  
847 0040-LaSIPS) managed by the French National Research Agency under the “Investissements  
848 d’avenir” program (ANR-11-IDEX-0003-02). The authors would like to thank Francois Brisset  
849 (ICMMO) and Thomas Reiss for technical assistance for SEM imaging.

850

### 851 References

852

853 An, B., & Wagner, H. D. (2016). Role of microstructure on fracture of dentin. *Journal of the*  
854 *Mechanical Behavior of Biomedical Materials*, 59, 527-537.

855

856 An, B., Xu, Y., & Zhang, D. (2017). Crack initiation and propagation in composite microstructure of  
857 dentin. *International Journal of Solids and Structures*, 110, 36-43.

858

859 Arganda-Carreras, I., Kaynig, V., Rueden, C., Eliceiri, K. W., Schindelin, J., Cardona, A., ... Seung, H. S.  
860 (2017). Trainable Weka Segmentation: A machine learning tool for microscopy pixel classification.  
861 *Bioinformatics*, 33(15), 2424–2426. <https://doi.org/10.1093/bioinformatics/btx180>

862 Arola, D., & Reprogl, R. K. (2005). Effects of aging on the mechanical behavior of human dentin.  
863 *Biomaterials*, 26(18), 4051–4061. <https://doi.org/10.1016/j.biomaterials.2004.10.029>

864 Arson, C., Yasothan, Y., Jeanneret, R., Benoit, A., Roubier, N., & Vennat, E. (2020). An alternative to

- 865 periodic homogenization for dentin elastic stiffness. *Journal of Mechanics in Medicine and*  
866 *Biology*. <https://doi.org/10.1142/S0219519419500817>
- 867 Bangerth W., Rannacher R. (2003). Adaptive Finite Element Methods for Solving Differential  
868 Equations, Birkhäuser.
- 869
- 870 Bar-On, B., & Daniel Wagner, H. (2012). Enamel and dentin as multi-scale bio-composites. *Journal of*  
871 *the Mechanical Behavior of Biomedical Materials*.  
872 <https://doi.org/10.1016/j.jmbbm.2012.03.007>
- 873 Christensen, R.M. (2005). Mechanics of composite materials, Dover.
- 874 Christensen, R. M. (2013). The theory of material failure, Oxford University Press.
- 875 Cioranescu, D., & Donato, P. (1999). An Introduction to Homogenization, Oxford Lecture Series in  
876 Mathematics and its Applications, vol. 17, Oxford University Press.
- 877 Garberoglio, R., & Brännström, M. (1976). Scanning electron microscopic investigation of human  
878 dentinal tubules. *Archives of Oral Biology*. [https://doi.org/10.1016/S0003-9969\(76\)80003-9](https://doi.org/10.1016/S0003-9969(76)80003-9)
- 879 Han, C. F., Wu, B. H., Chung, C. J., Chuang, S. F., Li, W. L., & Lin, J. F. (2012). Stress–strain analysis  
880 for evaluating the effect of the orientation of dentin tubules on their mechanical properties and  
881 deformation behavior. *Journal of the Mechanical Behavior of Biomedical Materials*, 12, 1-8.  
882
- 883 Iwamoto, N., & Ruse, N. D. (2003). Fracture toughness of human dentin. *Journal of Biomedical*  
884 *Materials Research - Part A*. <https://doi.org/10.1002/jbm.a.10005>
- 885 Kinney, J. H., Balooch, M., Marshall, G. W., & Marshall, S. J. (1999). A micromechanics model of the  
886 elastic properties of human dentine. *Archives of Oral Biology*, 44(10), 813–822.  
887 [https://doi.org/10.1016/S0003-9969\(99\)00080-1](https://doi.org/10.1016/S0003-9969(99)00080-1)
- 888 Kinney, J. H., Balooch, M., Marshall, S. J., Marshall, G. W., & Weihs, T. P. (1996). Hardness and  
889 young's modulus of human peritubular and intertubular dentine. *Archives of Oral Biology*,  
890 41(1), 9–13. [https://doi.org/10.1016/0003-9969\(95\)00109-3](https://doi.org/10.1016/0003-9969(95)00109-3)
- 891 Kinney, J. H., Oliveira, J., Haupt, D. L., Marshall, G. W., & Marshall, S. J. (2001). The spatial  
892 arrangement of tubules in human dentin. *Journal of Materials Science: Materials in Medicine*, 12(8),  
893 743-751.  
894
- 895 Kinney, J. H., Marshall, S. J., & Marshall, G. W. (2003). The mechanical properties of human dentin: a  
896 critical review and re-evaluation of the dental literature. *Critical Reviews in Oral Biology &*  
897 *Medicine*, 14(1), 13-29.
- 898 Kinney, J. H., Gladden, J. R., Marshall, G. E. A., Marshall, S. J., So, J. H., & Maynard, J. D. (2004).  
899 Resonant ultrasound spectroscopy measurements of the elastic constants of human  
900 dentin. *Journal of biomechanics*, 37(4), 437-441.
- 901 Lees, S., & Rollins Jr, F. R. (1972). Anisotropy in hard dental tissues. *Journal of Biomechanics*, 5(6),  
902 557-566.
- 903 Lu, X., Fernández, M. P., Bradley, R. S., Rawson, S. D., O'Brien, M., Hornberger, B., ... Withers, P. J.  
904 (2019). Anisotropic crack propagation and deformation in dentin observed by four-dimensional  
905 X-ray nano-computed tomography. *Acta Biomaterialia*.  
906 <https://doi.org/10.1016/j.actbio.2019.06.042>
- 907 Lu, X., Rawson, S. D., & Withers, P. J. (2018). Effect of hydration and crack orientation on crack-tip  
908 strain, crack opening displacement and crack-tip shielding in elephant dentin. *Dental Materials*.

- 909 <https://doi.org/10.1016/j.dental.2018.04.002>
- 910 Mandel, J. (1965). Generalisation de la theorie de plasticite de W. T. Koiter. *International Journal of*  
911 *Solids and Structures*. [https://doi.org/10.1016/0020-7683\(65\)90034-X](https://doi.org/10.1016/0020-7683(65)90034-X)
- 912 Mjör, I. A., & Nordahl, I. (1996). The density and branching of dentinal tubules in human teeth.  
913 *Archives of Oral Biology*. [https://doi.org/10.1016/0003-9969\(96\)00008-8](https://doi.org/10.1016/0003-9969(96)00008-8)
- 914 Pashley, D. H. (1989). Dentin: A dynamic substrate - A review. *Scanning Microscopy*.
- 915 Pilkey, W. D. (2005). *Formulas for Stress, Strain, and Structural Matrices Formulas for Stress, Strain,*  
916 *and Structural Matrices .2nd Edition* John Wiley & Sons
- 917 Pilkey, W. D., & Pilkey, D. F. (2008). Peterson's Stress Concentration Factors, Third Edition. In  
918 *Peterson's Stress Concentration Factors, Third Edition*. <https://doi.org/10.1002/9780470211106>
- 919 Qin, Q. H., & Swain, M. V. (2004). A micro-mechanics model of dentin mechanical properties.  
920 *Biomaterials*, 25(20), 5081–5090. <https://doi.org/10.1016/j.biomaterials.2003.12.042>
- 921 Sanchez-Palencia, E. (1980), *Non-homogeneous media and vibration theory*, Springer.
- 922 Schindelin, J., Arganda-Carreras, I., Frise, E., Kaynig, V., Longair, M., Pietzsch, T., ... Cardona, A. (2012).  
923 Fiji: An open-source platform for biological-image analysis. *Nature Methods*.  
924 <https://doi.org/10.1038/nmeth.2019>
- 925 Schneider, C. A., Rasband, W. S., & Eliceiri, K. W. (2012). NIH Image to ImageJ: 25 years of image  
926 analysis. *Nature Methods*. <https://doi.org/10.1038/nmeth.2089>
- 927 Seyedkavoosi, S., & Sevostianov, I. (2019). Multiscale micromechanical modeling of the elastic  
928 properties of dentin. *Journal of the Mechanical Behavior of Biomedical Materials*.
- 929 Vennat, E., Bogicevic, C., Fleureau, J. M., & Degrange, M. (2009). Demineralized dentin 3D porosity  
930 and pore size distribution using mercury porosimetry. *Dental Materials*.  
931 <https://doi.org/10.1016/j.dental.2008.12.002>
- 932 Vennat, E., Wang, W., Genthial, R., David, B., Dursun, E., & Gourrier, A. (2017). Mesoscale porosity at  
933 the dentin-enamel junction could affect the biomechanical properties of teeth. *Acta*  
934 *Biomaterialia*, 51, 418–432. <https://doi.org/10.1016/j.actbio.2017.01.052>
- 935 Wang, R., Niu, L., Li, Q., Liu, Q., & Zuo, H. (2017). The peritubular reinforcement effect of porous  
936 dentine microstructure. *PLoS ONE*. <https://doi.org/10.1371/journal.pone.0183982>
- 937 Wu H.-W., Mu B., (2003), On stress concentrations for isotropic/orthotropic plates and cylinders with  
938 a circular holes, *Composites, B*, 34, 127-134
- 939 Yoon, Y. J. (2013). Estimation of the elastic constants of dentin. *International Journal of Precision*  
940 *Engineering and Manufacturing*. <https://doi.org/10.1007/s12541-013-0043-9>
- 941 Zanette, I., Enders, B., Dierolf, M., Thibault, P., Gradl, R., Diaz, A., ... & Zaslansky, P. (2015).  
942 Ptychographic X-ray nanotomography quantifies mineral distributions in human dentine. *Scientific*  
943 *Reports*, 5, 9210.
- 944
- 945 Zienkiewicz, O.C., Chan A. H. C., Pastor M., Schrefler B. A., Shiomi T., (1999) *Computational*  
946 *Geomechanics*, Wiley.
- 947 Ziskind, D., Hasday, M., Cohen, S. R., & Wagner, H. D. (2011). Young's modulus of peritubular and  
948 intertubular human dentin by nano-indentation tests. *Journal of Structural Biology*, 174(1), 23–

949 30. <https://doi.org/10.1016/j.jsb.2010.09.010>

950